

Bulges of disk galaxies at intermediate redshifts. I.

Samples with and without bulges in the Groth Strip Survey

L. Domínguez-Palmero¹, M. Balcells¹, P. Erwin², M. Prieto^{1,3}, D. Cristóbal-Hornillos^{1,4}, M. C. Eliche-Moral^{1,5}, and R. Guzmán⁶

¹ Instituto de Astrofísica de Canarias, E-38200 La Laguna, Tenerife, Spain
e-mail: 1dp@iac.es e-mail: balcells@iac.es

² Max-Planck-Institut fuer extraterrestrische Physik, Giessenbachstrasse, D-85748 Garching, Germany

³ Departamento de Astrofísica, Universidad de La Laguna, La Laguna, E-38200 Tenerife, Spain

⁴ Instituto de Astrofísica de Andalucía, 18008 Granada, Spain

⁵ Departamento de Astrofísica y Ciencias de la Atmósfera, Facultad de C.C. Físicas, Universidad Complutense de Madrid, E-28040 Madrid, Spain

⁶ Department of Astronomy, University of Florida, 211 Bryant Space Science Center, Gainesville, FL 32611-2055, USA

Draft October 22, 2021

ABSTRACT

Context. Analysis of bulges to redshifts of up to $z \sim 1$ have provided ambiguous results as to whether bulges as a class are old structures akin to elliptical galaxies or younger products of the evolution of their host disks.

Aims. We aim to define a sample of intermediate- z disk galaxies harbouring central bulges, and a complementary sample of disk galaxies without measurable bulges. We intend to provide colour profiles for both samples, as well as measurements of nuclear, disk, and global colours, which may be used to constrain the relative ages of bulges and disks.

Methods. We select a diameter-limited sample of galaxies in images from the HST/WFPC2 (Wide-Field Planetary Camera 2 at the Hubble Space Telescope) Groth Strip survey, which is divided into two subsamples of higher and lower inclination to assess the role of dust in the measures quantities. Mergers are visually identified and excluded. We take special care to control the pollution by ellipticals. The bulge sample is defined with a criterion based on nuclear surface brightness excess over the inward extrapolation of the exponential law fitted to the outer regions of the galaxies. We extract colour profiles on the semi-minor axis least affected by dust in the disk, and measure nuclear colours at 0.85 kpc from the centre over those profiles. Disk colours are measured on major axis profiles; global colours are obtained from 2.6'' diameter apertures. Colour transformations and K-corrections are calculated using SEDs covering bands *UBVIJK*, from the GOYA photometric survey.

Results. We obtain a parent sample containing 248 galaxies with known redshifts, spectroscopic or photometric, spanning $0.1 < z < 1.2$. The bulge subsample comprises 54 galaxies (21.8% of the total), while the subsample with no measurable bulges is 55.2% of the total (137 galaxies). The remainder (23%) is composed of mergers. We list nuclear, disk, and global colours (observed and rest-frame) and magnitudes (apparent and absolute), as well as galaxy colour gradients for the samples with and without bulges, and make them available in electronic form*. We also provide images, colour maps, plots of spectral energy distributions, major-axis surface brightness profiles, and minor-axis colour profiles for both samples.

Key words. Galaxies:Bulges – Galaxies:Evolution – Galaxies:Formation – Galaxies:Fundamental Parameters – Galaxies:High-redshift – Galaxies:Photometry

1. Introduction

Bulges of spiral galaxies are central ingredients in the study of galaxy formation. Traditionally seen as elliptical galaxies that happen to live inside disks (Renzini 1999), bulges are still often used by modellers as yardsticks of the importance of violent processes vs gentle accretion in the mass assembly of galaxies (e.g., Kauffmann 1996; Cole et al. 2000; Sáiz et al. 2001). In the now termed ‘classical’ hypothesis, bulges form before disks, at high redshifts, via major mergers (Baugh et al. 1998) or primordial collapse (Eggen et al. 1962). Subsequently, a new disk forms out of the remaining gas. However, other hypotheses

have been presented for bulge formation (see Wyse et al. 1997; Kormendy & Kennicutt 2004, for two recent reviews). In a second scenario, bulges form after disks through bar instabilities (Pfenniger & Norman 1990), clumpy fragmentation of the existing disk (Noguchi 2000; Immeli et al. 2004), or other secular processes; see Athanassoula (2005) for a discussion of the relation of these processes to disky and peanut-shaped bulges. A related model posits that bulges may be the product of initial star formation in a galaxy, which proceeds until the bulge becomes massive enough to allow subsequent incoming gas to form a stable disk (van den Bosch 1998). Minor mergers probably have a role in the growth of bulges and disks (Aguerri et al. 2001; Abadi et al. 2003; Bournaud et al. 2005; Eliche-Moral et al. 2006a), leading perhaps to a coeval growth of both components.

Send offprint requests to: L. Domínguez-Palmero

* Tables A.1 to A.6 are available in electronic form at the CDS via anonymous ftp to cdsarc.u-strasbg.fr (130.79.128.5) or via <http://cdsweb.u-strasbg.fr/cgi-bin/qcat?J/A+A/>

Knowing the relative ages of bulges and disks is key to being able to falsify one or more of the hypothesis for bulge for-

mation. A prevalence of blue bulges would argue against an old formation age for bulges. In the disk instability model, blue, starbursting bulges would need to be found in sufficient quantities to account for the mass growth of today's massive, red bulges. The third scenario would be supported by the finding of similar colour for bulges and disks.

Usually, two approaches are followed for obtaining bulge ages and exploring mechanisms of bulge formation and evolution. The first is the study of kinematic, luminosities, colours, and chemical abundances of local bulges to recover the tracks of their evolution. The second is the analysis of global properties of galaxies at high redshifts with the aim of studying their evolution nearer the epoch at which bulges may have formed.

In the local Universe, Peletier & Balcells (1996) found that the age differences between bulges and disks was, in most cases, consistent with zero. Similarly, Bouwens et al. (1999) concluded that dating uncertainties prevent us from distinguishing between the various bulge formation models. Indeed, age dating of stellar populations has large uncertainties. In the present series of papers, we address the Peletier & Balcells (1996) study at redshift up to $z \sim 1$.

To study bulges at high redshift, we need large samples from deep images at high spatial resolution. Deep surveys with HST provide enough resolution to resolve big bulges at cosmological distances; e.g. at $z = 1$, a bulge with a size of 2 kpc subtends $0.26''$ about twice the point spread function (PSF) of the HST/WFPC2. But defining and characterising bulge components faces several practical difficulties derived from the properties of the imaging survey and the adopted selection criteria. First, pixelation and convolution with the PSF make the detection of small bulges difficult. Second, cosmological surface brightness dimming prevents detection of extended disks. Hence, samples selected by magnitude will favor compact, spheroidal galaxies, while diameter-limited selection will include only those bulges embedded in moderate- or high-surface brightness disks. Bulge-disk decompositions of the surface brightness profiles, already difficult in the local Universe, are made harder at high redshifts because bulges are not mapped with enough resolution and also sometimes because of the irregular morphologies of many disks. Moreover, the bulge colours based on bulge-disk decomposition have the additional problem of assigning a single representative colour for the bulges and for the disks. As the colour of the disk is usually not uniform, one can subtract from bulge region disk light that is too blue or to red, which biases the bulge colour.

Many recent studies of high-redshift galaxies are relevant to the formation of bulges (e.g., Marleau & Simard 1998; Menanteau et al. 2001; Ellis et al. 2001; Hammer et al. 2001; Simard et al. 2002; Conselice et al. 2004; Koo et al. 2005b,a; Elmegreen et al. 2007; MacArthur et al. 2007, to name just a few). The range of agreement and discrepancies between the conclusions of these studies is strongly affected by differences in sample selection and in the methodology to infer age information from the data. In the present paper, we approach the definition of bulge samples at high redshift in a complementary way to previous studies. The aim is to work with samples of disk galaxies, i.e., we focus on bulges residing inside disks. We then isolate samples with and without measurable bulges, obtain colour profiles, and measure nuclear, disk and global colours. Specifically, we work with a diameter-limited sample in the Groth Strip survey, divided in two subsamples by inclination. From those samples we exclude mergers (visually identified by their morphology), and take care to control sample pollution by bona-fide ellipticals, which should be minimised in the high-inclination sam-

ple. We define a prominence index η as the surface brightness excess over the inward extrapolation of the outer disk profile, and use it to identify the sample of galaxies with measurable bulges. As a result, we get the sample of intermediate- z bulge galaxies, but also we obtain a comparison sample of disk galaxies with no measurable bulges. We provide nuclear, disk, and global colours for galaxies in both samples in tabular form.

Details on the approach followed here are given in Sect. 2. Section 3 describes the HST and ground-based data. In Sect. 4, we describe the characteristics of the high- and low-inclination samples, compare different methods to select bulge sample and describe our bulge sample selection method, discuss completeness issues as well as comparison samples at intermediate redshifts in the same survey. Bulge and disk colour measurements and K-corrections are detailed in Sect. 5. The characteristics and colours of different galaxy samples with and without bulges are tabulated in Appendix A; in Appendix B, we show the HST/WFPC2 $F814W$ images, also colour maps, semi-major axis surface brightness profiles and semi-minor axis colour profiles of the bulge sample.

In a second paper (Dominguez-Palmero & Balcells 2008, hereafter Paper II), we will analyse the nuclear, disk, and global colours of the galaxies presented here, establish relations between different parameters, and discuss implications of the results for galaxy formation and evolution models. A cosmology with $\Omega_M = 0.3$, $\Omega_\Lambda = 0.7$, $H_0 = 70 \text{ km s}^{-1} \text{ Mpc}^{-1}$ is assumed throughout. Magnitudes are expressed in the Vega system.

2. Approach

The primary focus of the paper is on bulges residing in bona-fide disk galaxies. While there is sound evidence to assume strong similarities between (massive) bulges and ellipticals in the local Universe, we want to protect our high-redshift analysis from the biases derived from indiscriminately polluting our bulge samples with ellipticals.

Second, we want to control the effects of inclination on the colour measurements. For bona-fide bulges, i.e., those that protrude above the disk, and given sufficient spatial resolution, an inclined aspect is the safest aspect angle to measure colours in bulges. While inclined aspects are bad for disks because they enhance dust reddening, inclined views are superior for bulges because half the bulge is seen above the disk, where most of the dust resides. Measuring colours in this half and discarding the other one, we get reliable bulge colours with minimised dust reddening. This approach was used by Balcells & Peletier (1994) to define and provide colours for a reference sample of bulges in the local Universe. When applying this method to determine bulge colours at intermediate redshift, we face two limitations. First, when colour measurements are performed at galactocentric distances comparable to the size of the PSF, light from both sides of the centre gets convolved, and we risk losing the dust-free advantage provided by the inclined aspect angle. Second, when the objects we measure do not correspond to bona-fide bulges, but rather to those inner brightened disks that Kormendy (1993) named pseudobulges, then the inclined view is actually more prone to dust reddening than the face-on views. Given these difficulties, we design our experiment in a way that allows us to detect any effects of dust reddening, if present. Hence, we divide the initial parent sample in two subsamples with low ($< 50^\circ$) and high inclinations ($> 50^\circ$) and analyse them independently. Keeping the high- and low-inclination samples separate has the added advantage that sample pollution by ellipticals is almost non-existent in the high-inclination sample (see Sect. 4.3.1).

As our third starting point we work with direct colour measurements, rather than colour measurements derived from a bulge-disk decomposition of the galaxy images. Direct colour measurements suffer from disk contamination. But, in practice, colour gradients in disk galaxies are shallow, both in the local Universe (Peleterier & Balcells 1996) and at cosmologically-significant redshifts. Subtraction of disk light allows one to target fainter bulges but the dependence of the results on the bulge-disk modelling is difficult to predict, especially for high redshift galaxies which often depart from axisymmetry. Accounting for the colour gradients when modelling the profiles in two bands is challenging, hence it is common practice to assume uniform colours for the disk and for the bulge. However, in the common case of a global negative colour gradient, this will artificially redden the bulge colours. In our approach, we take advantage of the observation that galaxy colour profiles and colour maps show very small negative gradients in all semi-minor and semi-major axes. We therefore infer that the colours of the inner regions of the disk are very similar to those of the bulge and we do not correct our colour measurements from disk contamination. We provide checks on the amount of disk effects on the bulge colours by modelling the disk contribution under the assumption of uniform disk colours.

We finally assume that there is no unique way to correctly define a sample of bulges at high redshift. If our goal is to learn the ages of present-day bulges, we would need to include not only galaxies that look like bulges, but also all those galaxies that will grow bona fide bulges at lower redshifts than z_{obs} . Otherwise we will be biasing the sample of progenitors of present-day bulges in favor of the oldest progenitors (van Dokkum & Franx 2001). While a full treatment of such bias is beyond the scope of this work, we simply look for central light concentration as an indication that a bona fide bulge exists or may exist in the future. Using the observation that many disk galaxies show exponential surface brightness profiles (Freeman 1970), we define a bulge prominence index η that measures the excess central surface brightness over the inward extrapolation of the outer exponential profile and use it to select a sample of intermediate-redshift bulges. Such an index is a sort of concentration index, but is more sensitive to small bulges in extended disks than standard concentration indices (Abraham et al. 1996; Conselice et al. 2003) with which we compare the resulting selections.

The distance bias affecting the η index is similar to that of bulge-disk decompositions – small bulges are progressively missed as we move to higher z . We choose not to attempt any correction of that bias. We provide measurements for any bulge that is resolved by the HST/WFPC2 images, which is over two resolution elements. Distance and resolution effects need to be accounted for as part of the analysis of the results.

3. Data

3.1. HST imaging

Our intermediate- z galaxy samples were selected from the HST imaging of the Groth-Wesphal Strip (GWS; see, e.g., Groth et al. 1994; Roche et al. 1996). The GWS was included in the Medium-Deep Survey (MDS; see, e.g. Ratnatunga et al. 1999), and has been one of the main targets of the Deep Extragalactic Evolutionary Probe (DEEP; see, e.g., Simard et al. 2002). The original HST survey consists of 28 overlapping WFPC2 sub-fields covering a total area of 113 arcmin² in a 45'-long strip oriented NE to SW, with a position angle of 40°3'48" centred in RA(J2000) = 14^h16^m38.8^s, DEC(J2000) = 52°16'52.32", at

galactic latitude $b \sim 60^\circ$. For 27 of those fields, exposure times are 2800 s in the broad V filter ($F606W$) and 4400 s in the broad I filter ($F814W$). Field number 28, the fourth from the NW (Westphal Deep Field), has total exposures of 24400 s in $F606W$ and 25200 s in $F814W$.

The GWS HST data were obtained from the HST archive and were re-calibrated on-the-fly with the best reference files available at the CADC (Canadian Astronomy Data Center)¹. The calibration includes: flagging of static bad pixels, analog-to-digital (A/D) correction, subtraction of bias level, subtraction of bias image, subtraction of dark for exposures longer than 10 s, flat-field correction, shutter shading correction to exposures of less than 10 s, and computation of photometry keywords.

After that, we removed cosmic rays using the CRREJ task from the STSDAS.HST-CALIB.WFPC calibration package, and also corrected warm pixels in the images using the IRAF task COSMICRAYS, which replaces a detected warm pixel with the average of the four closest neighbors.

3.2. Ground-based optical-NIR imaging

We obtained ground-based imaging of the GWS from the GOYA (Galaxy Origins and Young Assembly) photometric survey. The GOYA photometric survey is a near-infrared (NIR) and optical survey in six broadband filters (U , B , $F606W$, $F814W$, J , K_s) covering, amongst other fields, the Groth strip, with target depths of $U=B=F606W=F814W=26$, and $J=K_s=22$ (AB mag). These data are taken in preparation for the GOYA project (Guzman 2003; Balcells 2003). GOYA is designed to exploit the NIR multi-object capabilities of the EMIR cryogenic spectrograph now under construction for the 10m GTC (see Balcells 1998; Balcells et al. 2000; Garzón et al. 2005, 2006), to carry out an extended census of the optical rest-frame spectra of $1 < z < 3$ galaxies.

The J - and K_s -band data for the Groth strip consist of dithered pointings with 96 min exposures in K_s and 32 min in J , with the INGRID Hawaii-1 camera on the William Herschel telescope (WHT) at the Observatorio Roque de los Muchachos (ORM). The 50% detection efficiencies range between $K_s = 21.24$ mag and $K_s = 20.21$ mag, depending on the seeing of the individual pointings. Details of the data reduction may be found in Cristóbal-Hornillos et al. (2003). U and B photometry are described in Eliche-Moral et al. (2006b). They were obtained with the WFC camera on the prime focus camera of the Isaac Newton Telescope (INT) at the ORM. Detection depths at the 50% efficiency were 24.83 mag and 25.45 mag in U and B , respectively.

With the combined HST and ground-based data, we derived broadband spectra energy distributions (SEDs) via the SExtractor package, using 2.6" circular apertures on images smoothed to a common 1.3" FWHM PSF (see Appendix B).

We selected best-fit SED templates for each source from those in the HYPERZ package (Bolzonella et al. 2000). We used such templates for photometric redshifts (Sect. 3.3) and K-corrections (Sect. 4.2 and Sect. 5.4).

3.3. Redshifts

More than 50% of the sources selected for this work (131 galaxies) have spectroscopic redshifts publically available as part of the DEEP1 data release of the DEEP Groth Strip Survey (GSS)²; see Weiner et al. (2005) for details on the determination of the

¹ <http://cadcwww.hia.nrc.ca>

² <http://deep.ucolick.org/>

redshifts. For the remainder of the objects, 117 galaxies, we derived photometric redshifts using HYPERZ v1.2. Photometry in the U , B , $F606W$, $F814W$, J , and K_s bands were fitted with template spectral energy distributions, using DEEP1 spectroscopic redshifts as a training set. The solutions show fractional errors $\langle|\Delta(z)|/(1+z)\rangle = 0.071$.

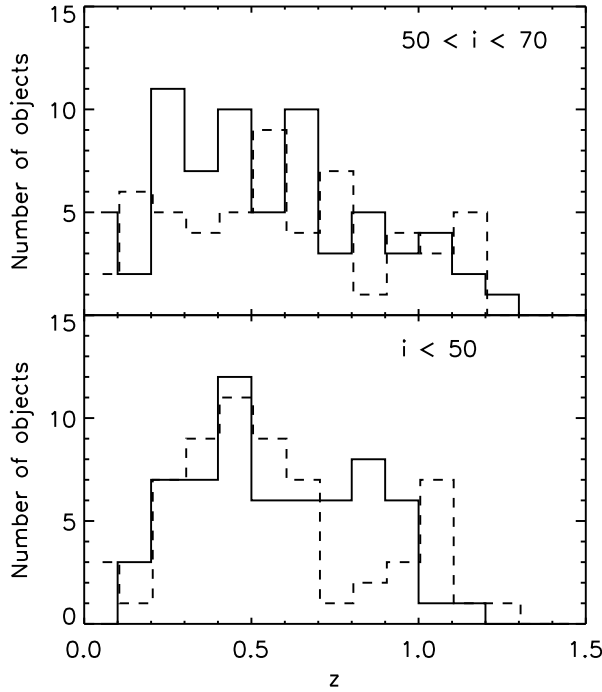


Fig. 1. Distribution of redshifts for the high-inclination and low-inclination samples. *Solid line*: spectroscopic redshifts. *Dashed line*: photometric redshifts.

4. Sample Selection

4.1. Disk galaxy sample

Following the ideas outlined in Sect. 2, we started by defining high-inclination and low-inclination samples on the GSS $F814W$ HST images. We divide the sample by inclination because we intend to study the possible effects of dust with inclination. We produced object catalogs with SExtractor version 2.3.2³ (Bertin & Arnouts 1996), using a detection threshold of 1.5σ and a detection minimum area of 16 pixels. We selected all galaxies with apparent major-axis radii $R > 1.4''$. The value of R corresponds to the semi-major axis of the ellipse that describes the isophotal limit of a detected object, it is calculated as three times the maximum spatial *rms* of the object profile along the semi-major axis, which is given by SExtractor `A_IMAGE` parameter. Working on galaxies with apparent diameter above a given limit provides sufficient resolution elements to map the bulge and disk components, and also helps to exclude compact, low-luminosity ellipticals from the sample. Our simulations show that $R > 1.4''$ cut is a good matches for the apparent sizes that

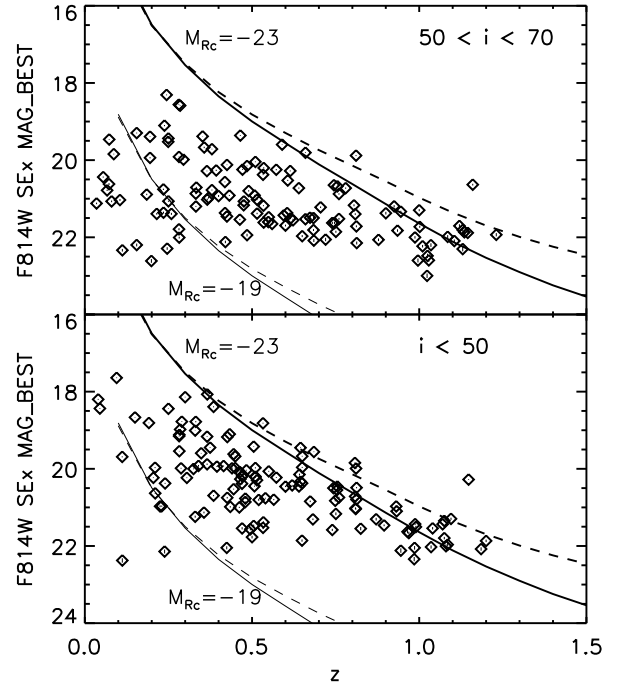


Fig. 2. Distribution of $F814W$ apparent magnitude (SExtractor MAG_BEST magnitudes) vs redshift for the high-inclination and low-inclination samples. *Thick solid and dashed lines*: apparent magnitude of Sa and Sd galaxy models (from GISSEL03 library, Bruzual & Charlot (2003); Chabrier (2003) IMF, solar metallicity and exponential SFR with $\tau = 3$ and 30 Gyr), respectively, for an R -band absolute magnitude equal to -23. *Thin lines*: the same but for $M_R = -19$.

large spirals in the local Universe would have if placed at the typical redshifts of our study. Additionally, a diameter-limited sample is easier to turn into a volume-limited sample, using V/V_{\max} techniques (Sect. 4.2).

The high-inclination sample was selected by applying a lower cut to the SExtractor ellipticity of 0.37, which corresponds to inclinations above 50° for disks. To avoid linear galaxies and edge-on disks, which pose specific problems for the data analysis, we excluded all galaxies with ellipticities above 0.66 (disk inclinations above 70°). After excluding those galaxies too close to the image edges and those with biased photometry, the resulting $50^\circ < i < 70^\circ$ sample contains 170 galaxies. Of those, 123 have redshift information, either spectroscopic or photometric (Sect. 3.3), and configure our parent inclined sample. The remaining 47 galaxies had no spectroscopic redshifts, and photometric redshifts were deemed unreliable due to lack of either UB or NIR photometry. Such cases were not included in the sample. In particular, there were 19 objects with no detection in U or B , or in both, and 24 that lack photometry in J or K , or in both. The remainder 4 galaxies belong to a field that was not observed in J .

As discussed in Sect. 2, the high-inclination selection of this sample should filter out most ellipticals, leaving a bona fide disk galaxy sample. The low-inclination sample was derived by selecting all galaxies with inclinations $i < 50^\circ$ from the $R > 1.4''$ diameter-limited catalog. This yielded 142 objects. Of

³ <http://terapix.iap.fr/soft/sextarator>

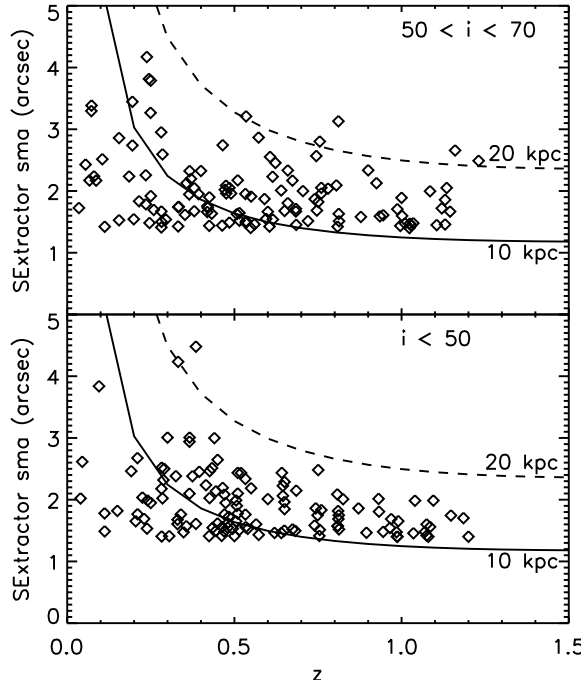


Fig. 3. Distribution of $F814W$ semi-major axis in arcsec (from SExtractor 'A-WORLD' size parameter) vs redshift for the high-inclination and low-inclination samples. *Solid line*: apparent size in arcsec for galaxies with a semi-major axis equal to 10 kpc. *Dashed lines*: the same for a semi-major axis equal to 20 kpc.

those, the 125 objects with known spectroscopic or photometric redshifts comprise the parent low-inclination sample. The remaining 17 galaxies were not included, as was done with the high-inclination sample, due to incomplete photometric coverage. There were 7 objects that lack UB photometry and 8 without data in NIR bands; 2 objects belong to the field not observed in J .

The redshift distributions of the high- and low-inclination samples are shown in Fig. 1. Redshifts, spectroscopic and photometric, cover the range $0.1 < z < 1.3$, the median values are equal to 0.53, for the high-inclination sample, and to 0.51, for the low-inclination one; the two distributions are statistically similar to one another, with a 45% probability of belonging to the same parent distribution, resulting from a K-S test.

Apparent magnitudes are in the range $18 < F814W < 23$ (Fig. 2). On the bright end, the upper envelope corresponds to Sa and Sd galaxy models with $M_R = -23$. The absolute magnitude corresponding to the faint end varies of course with redshift. Both high- and low-inclination samples extend down to $M_R = -19$ for $z < 0.5$, i.e., the magnitude domain of dwarf galaxies. Additionally, Fig. 2 shows that, at low redshifts ($z < 0.3$), the high-inclination sample reaches down to fainter magnitudes ($M_R \sim -16$) than the low-inclination sample. This difference is due to the higher surface brightness of inclined galaxies, which yields higher apparent sizes. These differences arise only for low-luminosity galaxies at low redshift, the dwarf domain we are not interested in. For brighter magnitudes, we see a marginal deficit of bright galaxies in the high-inclination sample

when compared to the low-inclination one, which may be due to higher extinction in highly-inclined objects. It is also possible that the brightest low-inclined objects at each redshift are massive spheroidal galaxies.

The distribution of the SExtractor apparent semi-major axes versus redshift is shown in Fig. 3. Solid and dashed lines represent the angular sizes corresponding to objects with physical sizes of 10 kpc and 20 kpc, respectively. Therefore, typical disk sizes are 10–15 kpc, except at $z < 0.3$ where many smaller objects enter into the samples. As expected, bigger sizes are found in the high-inclination sample due to the effect of inclination in the optical path, but the difference is small and we decided not to correct this effect.

4.2. Sample completeness

We use the V/V_{\max} formalism to assess the statistical completeness of our parent samples. To that end, we artificially shift each galaxy image over redshift, and determine the range of redshifts at which each galaxy would satisfy the size criteria we imposed on the original sample: $R > 1.4''$ i.e., the maximum distance of the galaxy to be included in the sample. Cosmological dimming, K-corrections, background brightness, pixelation, and image PSF are taken into account to mimic the $F814W$ HST/WFPC2 images of the Groth Strip, with K-corrections computed using best-fit SED templates (Bruzual & Charlot 2003) derived for each galaxy from HYPERZ best-fit solution.

To check that the sample is statistically complete, we have applied a V/V_{\max} test (Schmidt 1968; Thuan & Seitzer 1979), where V/V_{\max} is the ratio between the accessible volume of a galaxy and the maximum accessible volume for the same galaxy. For a randomly distributed sample of objects the mean value of V/V_{\max} should be $0.5 \pm 1/\sqrt{12 \times N}$, where N is the number of objects in the test. The average value we have obtained is $V/V_{\max} = 0.41 \pm 0.03$ and $V/V_{\max} = 0.42 \pm 0.03$, respectively, for the high- and low-inclination samples; thus, the sample has a mild bias toward nearby objects.

4.3. Galaxies with measurable bulges

In identifying and characterising bulge components in our parent galaxy sample, we face several practical difficulties. The first is spatial resolution: with HST/WFPC2, one $0.1''$ pixel projects onto 0.8 kpc at $z \sim 1$. As a result, many local bulges would become hidden within the central pixel if they were viewed at redshifts approaching $z = 1$. Second, we preferred to subtract the contribution from the disk, but bulge-disk decomposition, already an uncertain industry at low redshifts, is made difficult by the irregular morphologies of many high- z disks.

Given these difficulties, we tried five different methods and compared them to one another before adopting our bulge selection criterion. First, we carried out a bulge-disk decomposition with the two-dimensional fitting code of Trujillo et al. (2001). For the HST GSS images, simulations with synthetic data showed that the code provides reliable bulge structural parameters only for galaxies brighter than $F814W \approx 20$ mag, this is a limit too bright for our study. Our second and third methods are based on the Gim2D (Galaxy IMage 2D) bulge-disk decompositions from Simard et al. (2002), available from the DEEP public database. We defined samples using bulge-to-total ratios ($B/T > 0.4$), or bulge apparent magnitudes ($F814W < 23.57$); the latter criterion was used by Koo et al. (2005b). Our fourth method was based on concentration and asymmetry indices.

Early-type disk galaxies should have moderately high concentrations and low asymmetries (Bershady et al. 2000).

Our fifth method was the standard 'mark the disk' method of assuming an exponential profile for the disk, fitting it over some visually-chosen radial range, and selecting galaxies with central surface brightness excess over the inward extrapolation of the outer disk profile. We derived averaged profiles from 15° wedge-shaped apertures opening on both semi-major axes and fit an exponential law to the outer parts of the profiles. We defined the *prominence index* η as the difference between the measured central surface brightness and the extrapolated central surface brightness of the disk.

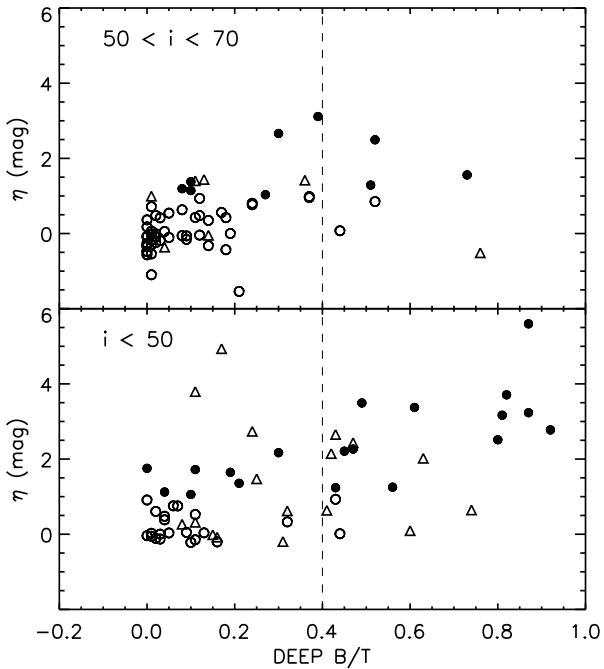


Fig. 4. Central prominence index η vs DEEP Gim2D bulge-to-total ratio for the high-inclination and low-inclination samples. *Filled circles*: galaxies with $\eta > 1$ (prominent bulges). *Open circles*: galaxies with $\eta < 1$. *Triangles*: galaxies morphologically classified as mergers.

After inspecting the surface brightness profiles of the sample galaxies, and analysing of how the properties of the bulge sample change with the η cutoff, we set a threshold of $\eta = 1$ mag to divide the sample into subsamples *with* and *without measurable bulges*. This was done both for the high- and low-inclination samples. In Fig. 7 we show two examples of galaxies with and without central excess belonging to the high-inclination sample.

Before segregating between bulge and non-bulge galaxies, we visually identified objects that could be morphologically classified as mergers, in both high- and low-inclination samples. Therefore, we have three subsamples in both low- and high-inclination samples.

The main difficulty with η criterion for bulge selection is its level of subjectivity when drawing the exponential fit to the outer profile. On the other hand, methods based on model fitting such as Gim2D impose model restrictions whose effects on the model uncertainties are also difficult to quantify. We argue that the η

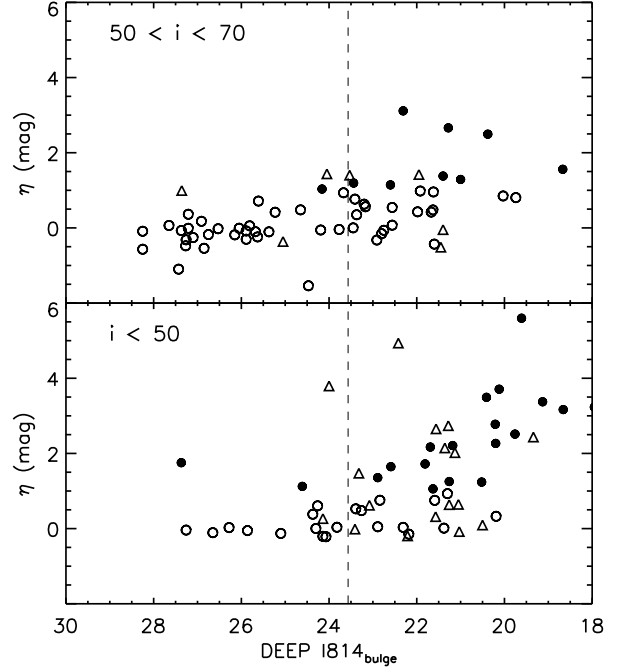


Fig. 5. Central prominence index η vs DEEP Gim2D apparent bulge $F814W$ magnitude for the high-inclination and low-inclination samples. *Filled circles*: galaxies with $\eta > 1$ (prominent bulges). *Open circles*: galaxies with $\eta < 1$. *Triangles*: galaxies morphologically classified as mergers.

method is simple, involves little modelling and can be verified individually through visual inspection of the profile whenever specific features need to be analysed.

We compare the various bulge sample selection methods outlined above in Figs. 4–6. In Fig. 4, we show our prominence index η versus B/T from Gim2D for those galaxies in our samples with a bulge-disk model in the DEEP database. As expected, most of the $\eta < 1$ galaxies show $B/T < 0.4$, a B/T range usually ascribed to disk-dominated galaxies. However, the $\eta \geq 1$ galaxies have B/T values ranging from 0 to 1. Hence, using our η criterion, we are able to select smaller- B/T galaxies than when a strict B/T cut is applied.

In Fig. 5, we compare the η selection with that based on bulge apparent $F814W$ magnitudes from the DEEP database. The limit value that Koo et al. (2005b) used to select their bulge sample was $F814W = 23.57$ in the Vega system. We see that most of our $\eta > 1$ galaxies have a DEEP bulge apparent $F814W$ magnitude brighter than the Koo et al. (2005b) cutoff, so both criteria coincide in this aspect, but there are also galaxies with $\eta < 1$ and mergers for which DEEP lists a bright bulge apparent magnitude. We interpret this as an indication that selecting by DEEP bulge magnitudes yields a sample that includes galaxies without bulge-disk structure, which we would classify in the non-bulge disk sample.

The distribution of the η -selected samples in the concentration-asymmetry plane is illustrated in Fig. 6. The region of low asymmetry and high concentration should be populated by early-type galaxies: E/S0/Sa/Sab. In the low-inclination sample, the concentration-asymmetry does select galaxies with $\eta > 1$. But for high-inclination galaxies the

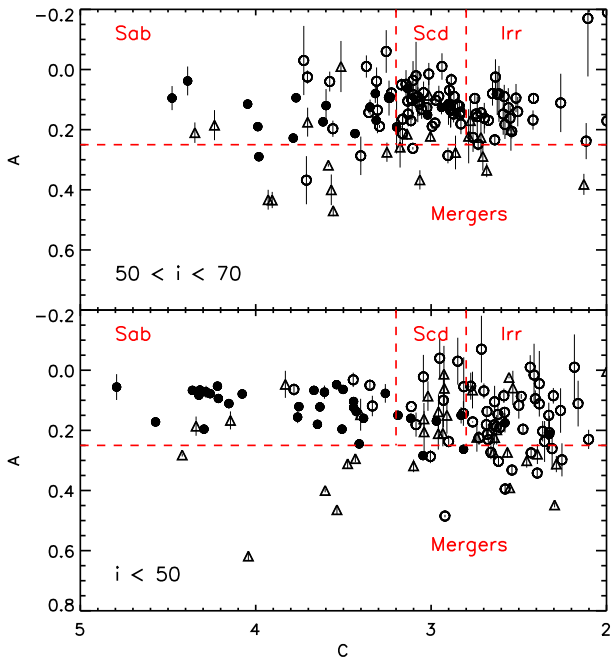


Fig. 6. Asymmetry-concentration diagram for the high-inclination and low-inclination samples. *Dashed lines* separate different A-C regions populated by different types of galaxies: E/S0/Sab, Scd, Irr, Mergers. *Filled circles*: galaxies with $\eta > 1$ (prominent bulges). *Open circles*: galaxies with $\eta < 1$. *Triangles*: galaxies morphologically classified as mergers.

method is of limited use as the concentration index does not discriminate well between galaxies with and without prominent bulges because of the high surface brightness of inclined disks. For low-inclination galaxies, the method has the additional problem of including bona fide ellipticals with the bulge sample, something we want to avoid, as discussed in Sect. 2.

4.3.1. Sample contamination by elliptical galaxies

After segregating between the three types of subsamples (bulge galaxies, non-bulge galaxies and mergers) we visually inspected the bulge sample to estimate the pollution of the sample by elliptical galaxies. While few ellipticals are expected in the high-inclination sample (the ellipticity cut allows only E7 galaxies), ellipticals may be present in the low-inclination sample. The criteria we used to identify them were the morphology as well as the surface brightness profiles and the photometric SEDs. We looked for galaxies with smooth structure, lack of evidence for spiral arms or localised star forming regions, with evidence of one single sersic surface brightness profile (no exponential outer component) and with very red SED typical of old populations. We find 5 possible elliptical candidates from 54 (9.3% of the bulge sample); all but one belong to the low-inclination sample. The id number of those objects are: 1138, 1137, 1113, 160, 1065.

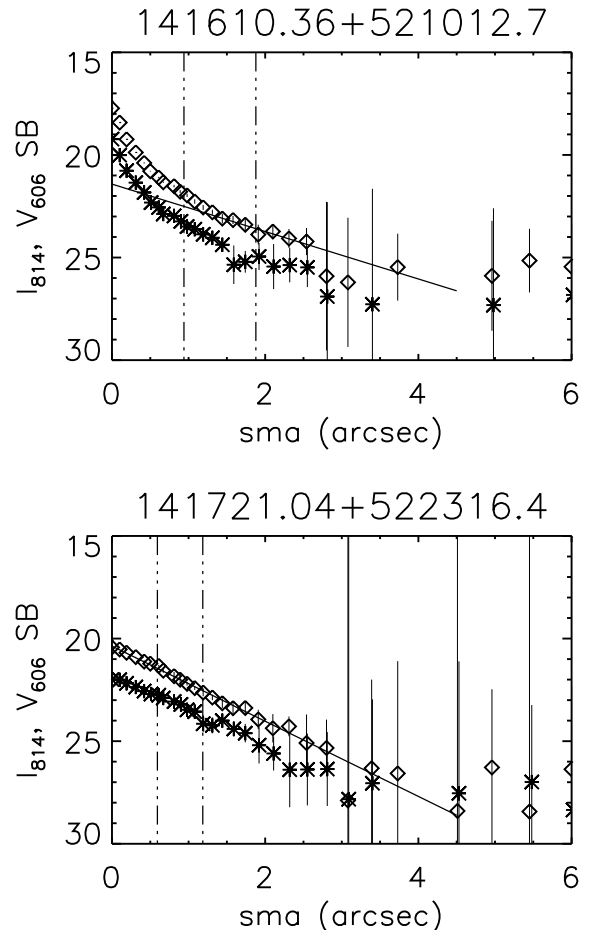


Fig. 7. Observed surface brightness averaged profiles derived from 15° wedge-shaped apertures over both semi-major axes. Diamonds: $F814W$ band. Asterisks: $F606W$ band. Both galaxies belong to the high-inclination sample. The *solid line* is the exponential law fit over the outer regions of the profiles. *Vertical dashed lines*: 1 and 2 times the scale length of the exponential law, respectively; range in which disk colours were measured. The upper galaxy has $\eta > 1$, while the lower one has $\eta < 1$.

5. Derivation of colours

5.1. Wedge colour profiles

For the derivation of bulge colours, we worked with colour profiles along wedge-shaped apertures opening on the minor axis. We chose this method, over the traditional one of using elliptically-averaged surface brightness profiles, to reduce the amount of reddening from dust in the disk, which can be quite important in inclined galaxies. A comparison of colour profiles along both semi-minor axes with wedges indicates which of the two bulge sides is reddened by the disk; this reddened side is discarded, and the bulge colour is extracted from the other profile. While we lose some signal with this method, for inclined galaxies the derived profiles gain reliability as dust reddening effects are greatly diminished. Even at intermediate redshifts, where the wedge method has some limitations (see Sect. 2), it is preferred to the ellipse method. For low-inclination galaxies, the differences are small.

Figure 8 shows an example of colour profiles of an inclined galaxy derived using wedges and using elliptically-averaged surface brightness profiles. The example shown ($\epsilon = 0.75$, disk inclination $i = 75^\circ$) is slightly above our high-inclination limit, and hence does not belong to our final sample; however, it provides a clear, extreme example of the effects of dust on bulge colours. In Fig. 8a, we show the $F814W$ -band image and the $(F606W - F814W)$ colour map in gray scale. Red linear bands along the galaxy disk to the left of the centre indicate that the disk lies in front of the bulge on the left side of the image. An elliptically-averaged colour profile, shown in Fig. 8b, shows a central region of red colours that would suggest the bulge region is distinctively redder than the disk; however, the minor-axis colour profiles (Fig. 8c) show that only one minor axis is redder than the disk, namely, the one to the left of the centre, in which the bulge is seen through the disk. Dust reddening is responsible for the redder colours; by measuring bulge colours on the side of the bulge that lies above the disk (to the right of the centre in Fig. 8a), dust reddening is largely avoided. Note that, in the case where the intrinsic colour structure of the galaxies consisted of (a) a red bulge surrounded by a disk with bluer populations, and (b) an opaque dust lane in the mid plane, with scale height much smaller than that of the stellar disk (a configuration studied by Tuffs et al. 2004; Möllenhoff et al. 2006), then dust would strongly attenuate half the galaxy light. However, it would only moderately redden the light that gets emitted on the near side of the galaxy. The result would be a colour asymmetry on the two semi-minor axes, but of opposite sign to the one due to dust described above, namely, the red side would correspond to the bulge. Such configuration does not seem to apply to hardly any of our galaxies, given that features in the colour maps do not follow the elliptical isophotes of the bulges, but tend to define linear patches corresponding to dust lanes (see Fig. 8a). The same was found at $z = 0$ in a similarly selected disk galaxy sample by Balcells & Peletier (1994): the redder semi-minor axis corresponds to the axis with the disk in front of the bulge.

The direction of the major axis was that given by SExtractor. Wedges on each semi-minor axis had an opening angle of 45° . The vertex of the wedges were placed at the centre of the $F814W$ galaxy image, as determined with the IRAF task IMCENTER. The $F814W$ and $F606W$ images are registered to within 0.24 pixels, and we did not correct for such small offcentring. The local background level was estimated with SExtractor using a background mesh width of 96 pixels and a local annulus thickness of 24 pixels.

Disk colours were similarly extracted from wedge apertures opening onto the major axis and with an aperture angle of 15° . Again, for inclined galaxies with dust in the disk, wedge apertures are preferred over the classical method of combining elliptically-averaged surface brightness profiles.

5.2. Nuclear colours

Throughout the paper, we will use local colours measured at fixed physical distances of 0.85 kpc from the centre, on the bluer semi-minor axis, as estimates of bulge colours. This distance is reasonably below the typical size of bulges, both in the local Universe (see Allen et al. 2006, for bulge-disk decompositions for the Millennium catalog) and at intermediate redshift in the Hubble Deep Field (HDF) (Trujillo & Aguerri 2004). The former finds that the main bulk of galaxies have bulges with $0.9 < R_{\text{eff}} < 4$ kpc, while Trujillo & Aguerri (2004) get a median R_{eff} of their bulges equal to 1.07 kpc. In addition, by measuring the colour at this galactocentric distance, we minimise the ef-

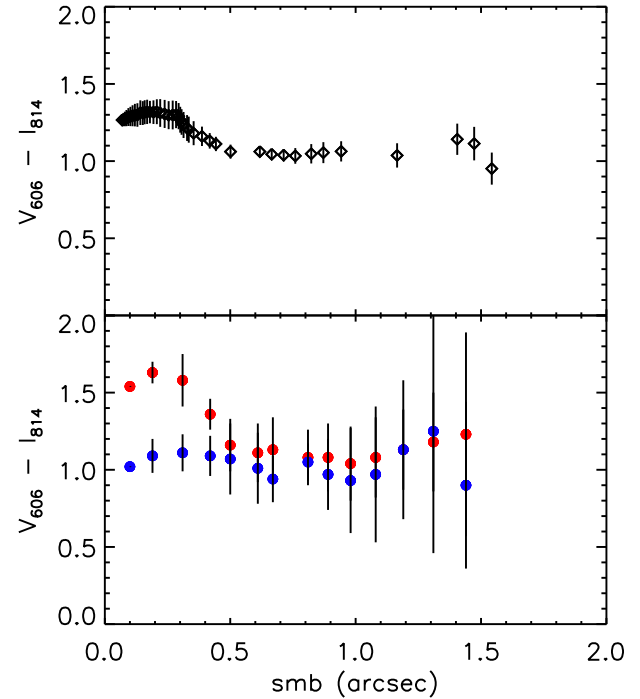
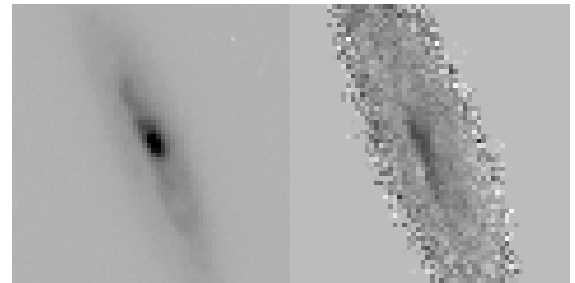


Fig. 8. (a) Surface brightness map and colour map for an inclined galaxy. The map side is $6''$. Darker areas correspond to brighter and redder regions, respectively. (b) Observed $(F606W - F814W)$ colour profile derived from a elliptically-averaged surface brightness profile. (c) Colour profiles derived along 40° wedge-shaped apertures opening on both semi-minor axes; red points: side reddened by dust in the disk; blue points: profile that diminishes dust reddening effect since its light is not seen through the disk.

fects of any residual reddening due to dust. The measured colour is close to the intrinsic colour of the stellar populations, since at 0.85 kpc from the centre, the stellar population scale height is still much larger than the one of the dust layer on the disk. We also measure the colour at the same galactocentric distance in the non-bulge sample, in order to compare the bulge and the non-bulge sample colours.

The physical distance 0.85 kpc corresponds to an angular size of $\sim 0.3''$ and $\sim 0.1''$ at $z = 0.15$ and $z = 1.2$, respectively. This radius lies very close to the centre for $z > 0.9$ and nuclear colours may be biased by the image PSF, however measurement of the PSF in the $F814W$ and $F606W$ WFPC2 GSS images revealed a median difference in PSF width of ~ 0.1 pixels. Due to the poor sampling of WFPC2 PSF (~ 1.4 pix per FWHM), we decided not to correct the PSF difference between $F814W$ and

$F606W$. We do not expect derived colours to be affected by such small PSF differences.

As already explained in Sect. 2, we do not apply any correction from disk light. Our results support this choice, as the colour structure of our galaxies does not correspond to a redder bulge surrounded by a uniformly bluer disk (see details of the analysis of colour profiles in Paper II, Sect. 4).

Globally, the wedge colours are slightly bluer than those derived from ellipse-fitting colour profiles. We show the colour differences (ellipse minus wedge) vs the galaxy inclination in Fig. 9. The scatter increases toward higher inclinations. We have calculated the median values of colour differences in galaxies with high central excess ($\eta > 1$) for three inclination bins, $i < 30^\circ$, $30^\circ < i < 55^\circ$, $55^\circ < i < 70^\circ$. We obtain for a distance from the centre equal to $0.1''$ 0.05, 0.12 and 0.08, with standard deviations 0.07, 0.12, 0.74, respectively. At $0.2''$ the median values and the standard deviations for the same inclination bins are, respectively, 0.13, 0.11, 0.06 and 0.12, 0.10, 0.57.

5.3. Disk colours and aperture colours

We estimate disk colours by averaging in the range from 1 to 2 times the scale length of the exponential law fit to the outer regions of the galaxies in the average of the profiles derived from wedge-shaped apertures over both semi-major axes. Contrary to bulges, which we expect to have bigger scale heights above the galaxy mid-plane, stars in disks are expected to be mixed with dust, and hence, the measured disk colours may be affected by dust reddening.

To obtain an estimate of the global galaxy colours, we use colours extracted from fixed circular apertures of diameter $2.6''$, on images that are smoothed to a common FWHM of $1.3''$. Such apertures fail to encompass the entire galaxies in some cases, but they provide representative global colours given the little light in the outer parts and the fact that colour gradients are very gentle. The comparison of global colours and disk colours with bulge colours is analysed in Paper II.

5.4. Colour transformations and absolute magnitude computation

We calculated K-corrections using SEDs covering bands $U, B, F606W, F814W, J$, and K_s from the GOYA photometric survey. Templates were obtained from the best-fit solutions delivered by HYPERZ, which was allowed to explore solutions over a narrow z range around the redshift of the galaxy.

Our approach differs from that of Koo et al. (2005b), who convert observed $(F606W - F814W)$ colours into rest-frame $(U - B)$ with parametric conversions derived from a subset (34 spectra) of an atlas of 43 spectra of local galaxies (Kinney et al. 1996). The use of theoretical SEDs from stellar population synthesis has potential disadvantages over the use of empirical models. Synthetic templates do not include factors that affect the SED, such as variation in metallicity and emission lines. Moreover, we are applying K-corrections, calculated from integrated SEDs of the whole galaxy, to both the bulge and the disk. However, for the galaxies in common with the sample of Koo et al. (2005b), a comparison of the K-corrections shows that differences are indeed small, with a standard deviation ~ 0.05 , which is dominated by our three reddest galaxies that are $\Delta(U - B) = 0.1$ mag redder than if we use Koo's K-corrections. The error in K-corrections derived from photomet-

ric redshift uncertainty and from SED choice have median values $\Delta K_{606} \sim 0.03$ and $\Delta K_{814} \sim 0.03$.

The $(U - B)$ and $(B - R)$ colour indices were chosen to provide rest-frame colour data. The index $(U - B)$ roughly coincides with observed $(F606W - F814W)$ at redshifts around $z \sim 0.8$, while $(B - R)$ matches the observed filters at redshifts around $z \sim 0.3$, near the low-end of our redshift range. With these choices, K-correction errors cancel out with SED colour errors. Additionally, much data is available on $(B - R)$ colours for galaxies in the local Universe, making the $(B - R)$ colour particularly useful. Therefore, throughout Paper II, all important relations will be shown in both $(U - B)$ and $(B - R)$. We will see that colour distributions in both sets of colours describe very similar patterns.

The colour transformations were done using the relations 1 and 2:

$$(U - B)^o = (F606W - F814W)^{\text{obs}} - K_{F606W} + K_{F814W} \\ + (U - F606W)_{\text{SED}}^o - (B - F814W)_{\text{SED}}^o \quad (1)$$

$$(B - R)^o = (F606W - F814W)^{\text{obs}} - K_{F606W} + K_{F814W} \\ + (B - F606W)_{\text{SED}}^o - (R - F814W)_{\text{SED}}^o \quad (2)$$

where the superindices o indicate that the parameter is in the rest frame of the galaxy, $(F606W - F814W)^{\text{obs}}$ is the colour in the observer's frame and $(U - F606W)_{\text{SED}}^o$, $(B - F814W)_{\text{SED}}^o$, $(B - F606W)_{\text{SED}}^o$ and $(R - F814W)_{\text{SED}}^o$ are the $(U - F606W)$, $(B - F814W)$, $(B - F606W)$ and $(R - F814W)$ colours in the rest frame, calculated by using the theoretical SED of the galaxy.

The error in $(U - B)$ and $(B - R)$ derived from K-correction errors and redshift uncertainty have median values $\Delta(U - B) \sim 0.15$ and $\Delta(B - R) \sim 0.12$. Those errors must be added in quadrature to the measured errors of the observed colours tabulated in Tables A.3 and A.4.

The absolute magnitudes are given by

$$M_i = m_i + 5 - 5 \log D_L - K_i \quad (3)$$

where M_i is absolute magnitude in i -band, m_i is apparent magnitude also in i band, D_L is the luminosity distance, and K_i is the K-correction in i band. The error in absolute magnitudes derived from redshift uncertainty and from SED choice have median values $\Delta M_B \sim 0.70$ and $\Delta M_R \sim 0.57$. This error must be added in quadrature to the measured errors of the observed magnitude m_i .

6. Results

We summarize the results of this paper in the Tables A.1, A.2, A.3, A.4, A.5, and A.6 in Appendix A. Tables A.1 and A.2 give basic source parameters for galaxies in the bulge sample and pure disk sample, respectively. We include the source ID, the redshift and redshift quality (Sect. 3.3), the galaxy semi-major axis and ellipticity (Sect. 4.1), the total apparent $F814W$ magnitude, and absolute magnitudes in Johnson-Cousins B and R . In these and the rest of the tables in Appendix A, galaxies are sorted in order of increasing redshift. Tables A.3 and A.4 list observed $(F606W - F814W)$ colours (Sects. 5.2, 5.3), as well as inferred rest-frame $(B - R)$, and $(U - B)$ colours (Sect. 5.4), for bulge (nucleus), disk, and galaxy for the samples with and without bulges, respectively. Finally, Tables A.5 and A.6 show the

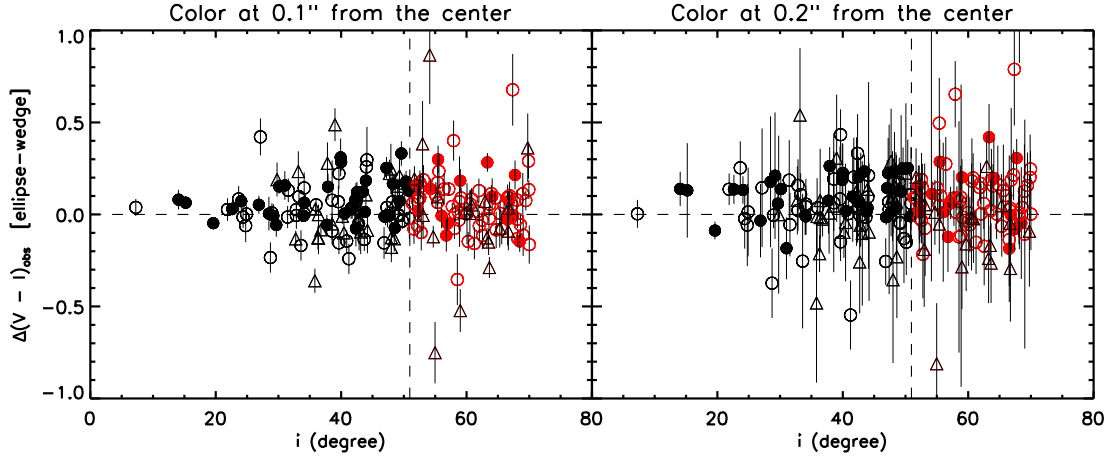


Fig. 9. Differences between colours calculated by ellipse method and the colours by wedge method at different distances from the centre (*left*: 0.1'', *right*: 0.2'') vs the galaxy inclination. *Filled circles*: colours of galaxies with $\eta > 1$, prominent bulges. *Open circles*: colours of galaxies with $\eta < 1$. *Triangles*: galaxies morphologically classified as mergers. The *vertical dashed line* separates the low- and high-inclination samples (*black* and *red* points, respectively, in the electronic format).

colour gradients for each galaxy in both semi-minor axes colour profiles and also in the averaged semi-major axis one.

Postage stamps, colour maps, spectral energy distributions, surface brightness, and colour profiles are provided for all of the sources in Appendix B. Colour profiles over the geometrically deprojected bluer semi-minor axes in kpc are shown in Appendix C.

The numbers of objects in each of our defined subsamples (see Sect. 4) are given in Table 1. The total sample is composed of 312 objects, of which 42% have spectroscopic redshifts and 37.5% have photometric redshifts. The main subsample of objects with known redshifts thus comprises 248 galaxies. Of these, 54 are disk galaxies with measurable bulges (21.8% of the sample with known redshift), 137 are bulgeless disk galaxies (55.2%), and 57 are mergers (23%). Four low-inclination galaxies and one high-inclination galaxy from the bulge sample (9.3%) are possible elliptical candidates. All subsamples include a number of dwarf galaxies, defined as having $M_B > -18$; the dwarf frequency is higher in the high-inclination subsample due to the higher surface brightness of inclined disks.

Table 1. Number of galaxies in each subsample

Sample	$i < 50$	$50 < i < 70$
$R > 1.4''$	142	170
z_{spec}	63	68
z_{phot}	62	55
$\eta > 1$ (bulges)	35	19
Ellipticals	4	1
Mergers	34	23
$\eta < 1$ (no bulges)	56	81
$M_B < -18$	5	14

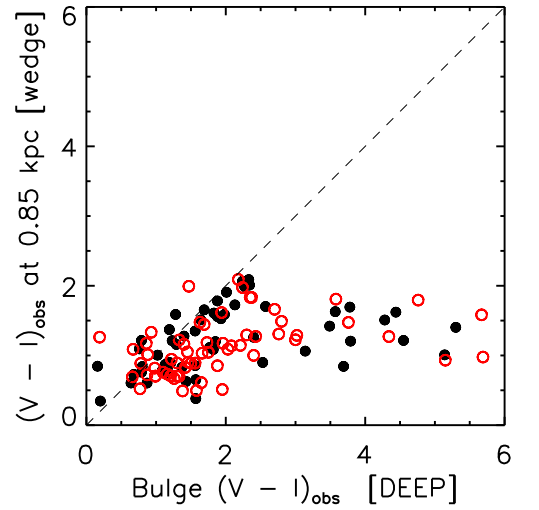


Fig. 10. Observed ($F606W - F814W$) wedge colour measured at 0.85 kpc vs integrated bulge colour from DEEP bulge-disk decomposition, for the 123 galaxies in our sample for which the DEEP database lists a bulge colour. *Filled circles*: galaxies from the low-inclination sample. *Open circles*: galaxies from the high-inclination sample.

6.1. External comparison

In Fig. 10, we show the differences between wedge nuclear colours and Gim2D bulge colours, available from the DEEP database, for the 123 galaxies in our total sample for which the DEEP database lists a bulge colour. For most galaxies, Gim2D colours are redder than our wedge colours. The main cloud of the distribution scatters within $0 < \Delta(F606W - F814W) < 1$, for those we get a median difference value equal to 0.28 and a standard deviation equal to 0.35. Such offset is significant. When converted to rest-frame ($U - B$) colours, it is larger than the

$\Delta(U - B) = 0.17$ reddening expected for passive evolution from $z = 1$ to $z = 0$ (assuming here $z_f = 3.0$; see Paper II, Sect. 7, Fig. 2).

Additionally, 30% of the galaxies have DEEP bulge colours dramatically redder than our colours ($\Delta(F606W - F814W) = 1 - 5$). Those are objects whose DEEP bulge colours have very large errors, > 1.2 mag, and we suspect that the bulge-disk decomposition is particularly unstable in those cases.

Even after excluding the highly-deviant cases, the colour differences between DEEP and us highlight the difficulties in assigning a single, representative colour for bulges of intermediate redshift galaxies. Part of the offset must come from the fact that, in the derivation of bulge colours in the DEEP database, disk light gets subtracted assuming a uniform colour for each component. Because, in fact, most galaxies show a negative colour gradient (bluer outward, see colour profiles in Appendix B), when assuming a uniform disk colour, one subtracts light that is too blue from the bulge region; this yields a bulge colour biased to the red. We made simple estimates of disk contamination under the assumption of an exponential disk with uniform colour. Colour corrections range from $\Delta(F606W - F814W) \sim 0.0$ for the highest η , up to $\Delta(F606W - F814W) \sim 0.5$ for $\eta \sim 1$: the mean bulge colour correction for the high- (low)-inclination subsamples is 0.13 (0.03).

Given that these corrections are smaller than the median colour difference between the DEEP measurement and ours, other processes may be at work. Plausibly, forcing a $R^{1/4}$ functional form for the bulge profile, and an exponential profile for the disk, might contribute to making the bulge redder as well. Conversely, our bulge colours may be biased to the blue if our wedge apertures happen to hit nuclear patches of star formation or, in cases in which the bulge side does not correspond to the bluest semi-minor axis (see Sect. 5.1).

7. Conclusions

We have presented a sample of 248 disk galaxies from the Groth strip with known redshifts in which we have identified candidate bulge components. We provide global photometry as well as colour measurements for bulges, disks, and for each galaxy as a whole. For galaxies without bulges, we provide colour measurements at the same radial distances and following the same method as done for the galaxies with bulges. These colours are analysed in Paper II. The tables in the Appendices are available in electronic format from the authors.

Acknowledgements. We thank the anonymous referee for suggestions that improved the paper and Ignacio Trujillo, Carlos López, David Abreu, Marc Vallbé, Enrique García-Dabó, Alfonso Aragón-Salamanca, David Koo, and Reynier Peletier, for useful discussions. This work was supported by the Spanish Programa Nacional de Astronomía y Astrofísica through project number AYA2006-12955. Some/all of the data presented in this paper were obtained from the Multimission Archive at the Space Telescope Science Institute (MAST). STScI is operated by the Association of Universities for Research in Astronomy, Inc., under NASA contract NAS5-26555. Support for MAST for non-HST data is provided by the NASA Office of Space Science via grant NAG5-7584 and by other grants and contracts. This work uses data obtained with support of the National Science Foundation grants AST 95-29028 and AST 00-71198.

References

- Abadi, M. G., Navarro, J. F., Steinmetz, M., & Eke, V. R. 2003, ApJ, 591, 499
- Abraham, R. G., Tanvir, N. R., Santiago, B. X., et al. 1996, MNRAS, 279, L47
- Aguerri, J. A. L., Balcells, M., & Peletier, R. F. 2001, A&A, 367, 428
- Allen, P. D., Driver, S. P., Graham, A. W., et al. 2006, MNRAS, 371, 2
- Athanassoula, E. 2005, MNRAS, 358, 1477
- Balcells, M. 1998, Ap&SS, 263, 361
- Balcells, M. 2003, in Revista Mexicana de Astronomía y Astrofísica Conference Series, Vol. 16, Science with the GTC, ed. J. M. Rodriguez Espinoza, F. Garzon Lopez, & V. Melo Martin, 69–72
- Balcells, M., Guzman, R., Patron, J., et al. 2000, in the Society of Photo-Optical Instrumentation Engineers (SPIE) Conference, Vol. 4008, Optical and IR Telescope Instrumentation and Detectors, ed. M. Iye & A. F. Moorwood, 797–805
- Balcells, M., & Peletier, R. F. 1994, AJ, 107, 135
- Baugh, C. M., Cole, S., Frenk, C. S., & Lacey, C. G. 1998, ApJ, 498, 504
- Bershady, M. A., Jangren, A., & Conselice, C. J. 2000, AJ, 119, 2645
- Bertin, E., & Arnouts, S. 1996, A&AS, 117, 393
- Bolzonella, M., Miralles, J.-M., & Pelló, R. 2000, A&A, 363, 476
- Bournaud, F., Jog, C. J., & Combes, F. 2005, A&A, 437, 69
- Bouwens, R., Cayón, L., & Silk, J. 1999, ApJ, 516, 77
- Bruzual, G., & Charlot, S. 2003, MNRAS, 344, 1000
- Chabrier, G. 2003, PASP, 115, 763
- Cole, S., Lacey, C. G., Baugh, C. M., & Frenk, C. S. 2000, MNRAS, 319, 168
- Conselice, C. J., Bershady, M. A., Dickinson, M., & Papovich, C. 2003, AJ, 126, 1183
- Conselice, C. J., Grogin, N. A., Jogee, S., et al. 2004, ApJ, 600, L139
- Cristóbal-Hornillos, D., Balcells, M., Prieto, M., et al. 2003, ApJ, 595, 71
- Dominguez-Palmero, L., & Balcells, M. 2008, submitted to A&A
- Eggen, O. J., Lynden-Bell, D., & Sandage, A. R. 1962, ApJ, 136, 748
- Eliche-Moral, M. C., Balcells, M., Aguerri, J. A. L., & González-García, A. C. 2006a, A&A, 457, 91
- Eliche-Moral, M. C., Balcells, M., Prieto, M., et al. 2006b, ApJ, 639, 644
- Ellis, R. S., Abraham, R. G., & Dickinson, M. 2001, ApJ, 551, 111
- Elmegreen, D. M., Elmegreen, B. G., Ravindranath, S., & Coe, D. A. 2007, ApJ, 658, 763
- Freeman, K. C. 1970, ApJ, 160, 811
- Garzón, F., Abreu, D., Barrera, S., et al. 2006, in the Society of Photo-Optical Instrumentation Engineers (SPIE) Conference, Vol. 6269, Ground-based and Airborne Instrumentation for Astronomy. Proceedings of the SPIE, ed. I. S. McLean & M. Iye, 626918
- Garzón, F., Abreu, D., Barrera, S., et al. 2005, in Revista Mexicana de Astronomía y Astrofísica Conference Series, Vol. 24, II International GTC Workshop: Science with GTC 1st-light Instruments and the LMT, ed. A. M. Hidalgo-Gámez, J. J. González, J. M. Rodríguez Espinosa, & S. Torres-Peimbert, 21–28
- Groth, E. J., Kristian, J. A., Lynds, R., et al. 1994, in Bulletin of the American Astronomical Society, Vol. 26, American Astronomical Society, 185th AAS Meeting, 1403–+
- Guzman, R. 2003, in Revista Mexicana de Astronomía y Astrofísica Conference Series, Vol. 16, Science with the GTC, ed. J. M. Rodriguez Espinoza, F. Garzon Lopez, & V. Melo Martin, 209–212
- Hammer, F., Gruel, N., Thuan, T. X., Flores, H., & Infante, L. 2001, ApJ, 550, 570
- Immeli, A., Samland, M., Gerhard, O., & Westera, P. 2004, A&A, 413, 547
- Kauffmann, G. 1996, MNRAS, 281, 487
- Kinney, A. L., Calzetti, D., Bohlin, R. C., et al. 1996, ApJ, 467, 38
- Koo, D. C., Datta, S., Willmer, C. N. A., et al. 2005a, ApJ, 634, L5
- Koo, D. C., Simard, L., Willmer, C. N. A., et al. 2005b, ApJS, 157, 175
- Kormendy, J. 1993, in International Astronomical Union. Symposium, Kluwer Academic Publishers, Vol. 153, Galactic bulges: proceedings of the 153rd Symposium of the International Astronomical Union, ed. H. Dejonghe & H. J. Habing, 209–+
- Kormendy, J., & Kennicutt, Jr., R. C. 2004, ARA&A, 42, 603
- MacArthur, L. A., Ellis, R. S., Treu, T., et al. 2007, submitted to ApJ, (arXiv:0711.0238)
- Marleau, F. R., & Simard, L. 1998, ApJ, 507, 585
- Menanteau, F., Abraham, R. G., & Ellis, R. S. 2001, MNRAS, 322, 1
- Möllenhoff, C., Popescu, C. C., & Tuffs, R. J. 2006, A&A, 456, 941
- Noguchi, M. 2000, MNRAS, 312, 194
- Peletier, R. F., & Balcells, M. 1996, AJ, 111, 2238
- Pfenniger, D., & Norman, C. 1990, ApJ, 363, 391
- Ratnatunga, K. U., Griffiths, R. E., & Ostrander, E. J. 1999, AJ, 118, 86
- Renzini, A. 1999, in When and How do Bulges Form and Evolve?, ed. C. M. Carollo, H. C. Ferguson, & R. F. G. Wyse, Cambridge University Press, 9–+
- Roche, N., Ratnatunga, K., Griffiths, R. E., Im, M., & Neuschaefer, L. 1996, MNRAS, 282, 1247
- Sáiz, A., Domínguez-Tenreiro, R., Tissera, P. B., & Courteau, S. 2001, MNRAS, 325, 119
- Schmidt, M. 1968, ApJ, 151, 393
- Simard, L., Willmer, C. N. A., Vogt, N. P., et al. 2002, ApJS, 142, 1
- Thuan, T. X., & Seitzer, P. O. 1979, ApJ, 231, 680
- Trujillo, I., & Aguerri, J. A. L. 2004, MNRAS, 355, 82
- Trujillo, I., Aguerri, J. A. L., Gutiérrez, C. M., & Cepa, J. 2001, AJ, 122, 38

- Tuffs, R. J., Popescu, C. C., Völk, H. J., Kylafis, N. D., & Dopita, M. A. 2004,
A&A, 419, 821
van den Bosch, F. C. 1998, ApJ, 507, 601
van Dokkum, P. G. & Franx, M. 2001, ApJ, 553, 90
Weiner, B. J., Phillips, A. C., Faber, S. M., et al. 2005, ApJ, 620, 595
Wyse, R. F. G., Gilmore, G., & Franx, M. 1997, ARA&A, 35, 637

Appendix A: Data tables

Notes for Tables A.1 and A.2:

- (1) Source number identification
- (2) Source ID, given by sky coordinates of the source: RA+DEC
- (3) Source redshift
- (4) Redshift quality: 1 - spectroscopic, 2 - photometric
- (5) Source semi-major axis in arcsec from SExtractor "A" size parameter
- (6) Source ellipticity from SExtractor ($1 - b/a$)
- (7) Subsample from which the source comes: hi - high-inclination sample, li - low-inclination sample
- (8) Total $F814W$ magnitude of galaxy from SExtractor MAG_BEST magnitude)
- (9) Galaxy absolute magnitude in B -band
- (10) Galaxy absolute magnitude in R -band

Note for columns 9–10: The total errors in galaxy absolute magnitude, ΔM_B and ΔM_R , come from the sum in quadrature of the measured error in observed $F814W$ magnitude and the error derived from redshift uncertainty and SED choice (see Sect. 5.4).

Notes for Tables A.3 and A.4:

- (1) Source number identification
- (2) Observed nuclear ($F606W - F814W$) colour, measured at 0.85 kpc from the centre
- (3) Observed disk ($F606W - F814W$) colour, measured in the range between 1 and 2 times the scale length of the exponential law fit to the outer regions of the galaxies
- (4) Observed global ($F606W - F814W$) colour, measured within a 2.6'' diameter aperture
- (5) Rest-frame nuclear ($U - B$) colour
- (6) Rest-frame disk ($U - B$) colour
- (7) Rest-frame global ($U - B$) colour
- (8) Rest-frame nuclear ($B - R$) colour.
- (9) Rest-frame disk ($B - R$) colour
- (10) Rest-frame global ($B - R$) colour

Note for columns 5–10: The total errors in rest-frame colours, $\Delta(U - B)$ and $\Delta(B - R)$, come from the sum in quadrature of the measured error in ($F606W - F814W$) colour and the error derived from the colour transformation (see Sect. 5.4).

Notes for Tables A.5 and A.6:

- (1) Source number identification
- (2) Colour gradient calculated over the bluer deprojected semi-minor axes colour profile
- (3) Colour gradient calculated over the redder deprojected semi-minor axes colour profile
- (4) Colour gradient calculated over the averaged semi-major axes colour profile

Note for columns 2–4: The colour gradients are measured in magnitudes per deprojected kpc. The errors are the 1-sigma uncertainty estimates for the returned parameters of the linear fits.

Table A.1. Bulge sample data

No. (1)	Source ID (2)	z (3)	Qz (4)	R (arcsec) (5)	ϵ (6)	Sample (7)	I_{814} (8)	M_B (9)	M_R (10)
1131	141707.44+522439.8	0.045	2	2.62	0.28	li	18.44 ± 0.01	-16.89	-17.63
1139	141524.68+520554.1	0.095	2	3.84	0.24	li	17.64 ± 0.01	-18.72	-20.04
1078	141611.84+521312.2	0.1118	1	1.78	0.09	li	19.69 ± 0.01	-17.41	-18.42
1081	141646.71+521930.3	0.15	2	1.82	0.33	li	18.67 ± 0.01	-18.70	-20.10
1125	141624.06+521517.0	0.1915	1	2.46	0.04	li	18.81 ± 0.01	-19.19	-20.56
139	141547.15+520610.5	0.235	2	2.26	0.52	hi	20.76 ± 0.02	-18.11	-19.14
170	141724.80+522553.5	0.2381	1	4.17	0.39	hi	19.10 ± 0.02	-20.03	-20.83
159	141718.47+522419.7	0.2811	1	2.95	0.39	hi	18.56 ± 0.01	-20.41	-21.82
1005	141537.95+520408.3	0.2826	1	1.41	0.33	li	19.54 ± 0.01	-19.55	-20.84
1099	141532.40+520321.4	0.285	2	2.02	0.14	li	18.98 ± 0.01	-20.28	-21.42
47	141557.65+520806.1	0.295	2	1.54	0.62	hi	19.99 ± 0.01	-19.00	-20.52
1138	141648.92+521738.2	0.3	2	3.01	0.32	li	18.14 ± 0.01	-20.89	-22.42
1063	141535.07+520305.6	0.33	2	1.68	0.27	li	19.01 ± 0.00	-20.53	-21.78
1020	141729.67+522759.1	0.3481	1	1.47	0.06	li	19.60 ± 0.01	-20.57	-21.26
1135	141637.99+521542.0	0.3656	1	2.94	0.35	li	19.16 ± 0.01	-20.73	-21.91
1137	141620.36+521349.4	0.366	1	3.01	0.26	li	18.07 ± 0.00	-21.68	-23.05
1118	141644.32+521654.4	0.3745	1	2.38	0.28	li	19.45 ± 0.01	-20.81	-21.61
1142	141640.99+521806.6	0.385	2	4.48	0.17	li	18.39 ± 0.01	-21.70	-22.82
104	141530.79+520549.3	0.425	2	1.90	0.61	hi	20.12 ± 0.01	-20.04	-21.45
1108	141542.78+520731.4	0.445	2	2.14	0.17	li	19.62 ± 0.01	-20.67	-22.08
1057	141531.06+520319.3	0.4495	1	1.62	0.36	li	19.68 ± 0.01	-20.70	-22.02
1046	141723.69+522511.3	0.4635	1	1.56	0.26	li	20.08 ± 0.01	-20.36	-21.71
155	141702.24+522236.1	0.465	2	2.74	0.46	hi	19.36 ± 0.01	-21.08	-22.48
1024	141557.32+520824.7	0.47	2	1.48	0.11	li	20.19 ± 0.01	-20.63	-21.50
1068	141615.28+521233.5	0.4832	1	1.73	0.34	li	20.03 ± 0.01	-20.75	-21.83
123	141517.13+520218.1	0.485	1	2.05	0.42	hi	20.15 ± 0.01	-20.72	-21.66
1093	141700.67+521918.4	0.505	2	1.99	0.13	li	19.42 ± 0.01	-21.56	-22.50
134	141528.72+520611.0	0.51	2	2.17	0.62	hi	20.04 ± 0.01	-20.74	-22.02
1077	141712.28+522205.2	0.51	2	1.78	0.35	li	20.22 ± 0.01	-20.44	-21.89
1122	141545.37+520626.6	0.51	2	2.44	0.14	li	19.97 ± 0.02	-20.93	-22.02
1033	141511.65+520046.4	0.5148	1	1.51	0.37	li	20.29 ± 0.01	-20.44	-21.84
1117	141639.99+521735.0	0.5328	1	2.34	0.21	li	18.82 ± 0.01	-22.03	-23.45
110	141627.43+521351.1	0.533	1	1.95	0.55	hi	20.38 ± 0.01	-20.84	-21.63
162	141711.05+522331.1	0.535	2	3.21	0.63	hi	20.20 ± 0.02	-20.79	-22.03
102	141610.36+521012.7	0.59	2	1.87	0.43	hi	19.60 ± 0.01	-21.68	-22.86
1017	141752.99+522838.4	0.62	2	1.46	0.23	li	20.43 ± 0.01	-21.12	-22.10
116	141611.98+521347.1	0.6399	1	2.01	0.56	hi	20.72 ± 0.01	-20.78	-22.11
1113	141715.32+522532.7	0.645	2	2.23	0.32	li	19.45 ± 0.01	-22.08	-23.34
1083	141615.03+521121.7	0.65	2	1.85	0.23	li	19.67 ± 0.01	-21.86	-23.26
1115	141547.12+520823.3	0.65	2	2.29	0.32	li	19.96 ± 0.01	-21.67	-22.82
142	141742.15+523025.2	0.6597	1	2.33	0.44	hi	19.81 ± 0.01	-21.93	-22.97
1036	141809.09+523159.4	0.674	1	1.52	0.13	li	20.84 ± 0.02	-21.04	-21.75
1028	141632.93+521601.3	0.6821	1	1.50	0.26	li	21.31 ± 0.02	-20.50	-21.59
150	141646.96+521659.0	0.745	2	2.57	0.60	hi	20.65 ± 0.02	-21.42	-22.83
1034	141748.27+523117.2	0.7554	1	1.51	0.08	li	20.46 ± 0.02	-21.67	-22.84
1048	141649.88+521809.2	0.8084	1	1.57	0.21	li	20.72 ± 0.02	-21.68	-22.81
8	141651.57+522055.9	0.8087	1	1.42	0.45	hi	21.40 ± 0.02	-21.01	-22.42
160	141735.73+522645.5	0.811	1	3.13	0.49	hi	19.88 ± 0.01	-22.53	-23.75
1065	141538.89+520506.5	0.811	1	1.69	0.03	li	19.99 ± 0.01	-22.43	-23.80
1035	141620.52+521407.3	0.8126	1	1.52	0.25	li	20.49 ± 0.02	-21.94	-23.24
129	141603.04+521239.3	0.925	2	2.13	0.43	hi	21.19 ± 0.03	-21.81	-23.06
1097	141627.46+521453.5	0.9311	1	2.01	0.12	li	20.97 ± 0.03	-21.94	-22.75
59	141728.98+522422.6	0.945	2	1.61	0.46	hi	21.33 ± 0.02	-21.80	-23.13
1	141728.69+522538.3	1.0235	1	1.40	0.65	hi	23.00 ± 0.06	-20.35	-21.30

Table A.2. Non-bulge sample data

No. (1)	Source ID (2)	z (3)	Qz (4)	R (arcsec) (5)	ϵ (6)	Sample (7)	I_{814} (8)	M_B (9)	M_R (10)
86	141609.29+521058.8	0.035	2	1.73	0.46	hi	21.12 ± 0.02	-13.57	-14.37
1098	141633.59+521553.5	0.04	2	2.02	0.16	li	18.20 ± 0.01	-16.72	-17.57
133	141733.11+522825.1	0.0667	1	2.17	0.49	hi	20.78 ± 0.02	-15.28	-16.20
164	141725.18+522716.7	0.0723	1	3.30	0.47	hi	20.62 ± 0.02	-15.82	-16.53
165	141525.60+520334.0	0.0728	1	3.38	0.59	hi	19.46 ± 0.01	-16.71	-17.66
138	141740.55+522619.8	0.08	1	2.24	0.58	hi	21.07 ± 0.02	-15.81	-16.36
131	141538.06+520529.0	0.0866	1	2.17	0.48	hi	19.84 ± 0.01	-16.91	-17.72
148	141652.56+522049.9	0.105	2	2.52	0.50	hi	21.03 ± 0.02	-16.33	-16.99
1025	141613.94+521401.8	0.112	1	1.49	0.36	li	22.37 ± 0.06	-15.09	-15.80
9	141605.84+521129.0	0.1122	1	1.42	0.64	hi	22.34 ± 0.03	-15.09	-15.82
43	141538.67+520416.1	0.155	2	1.53	0.52	hi	22.20 ± 0.04	-15.91	-16.71
157	141518.03+520442.8	0.155	2	2.86	0.63	hi	19.30 ± 0.01	-18.83	-19.62
137	141540.28+520811.1	0.185	2	2.24	0.39	hi	20.89 ± 0.02	-17.78	-18.45
166	141602.91+520950.6	0.195	2	3.45	0.65	hi	19.94 ± 0.02	-18.82	-19.52
154	141606.59+521300.6	0.195	2	2.74	0.47	hi	19.39 ± 0.01	-19.00	-20.05
48	141625.85+521505.4	0.1991	1	1.54	0.64	hi	22.61 ± 0.05	-16.26	-16.89
1061	141640.37+521753.4	0.205	2	1.65	0.09	li	20.23 ± 0.01	-18.56	-19.34
1134	141544.58+520533.3	0.21	2	2.67	0.37	li	19.97 ± 0.01	-18.62	-19.65
1076	141723.35+522654.0	0.2105	1	1.77	0.32	li	20.63 ± 0.01	-18.16	-19.00
1066	141523.42+520430.7	0.23	2	1.69	0.35	li	20.97 ± 0.02	-18.10	-18.88
93	141740.23+523016.4	0.2353	1	1.79	0.43	hi	21.36 ± 0.02	-17.71	-18.55
1039	141525.58+520504.5	0.2385	1	1.53	0.18	li	22.14 ± 0.05	-17.06	-17.79
1094	141638.51+521715.9	0.24	2	1.99	0.34	li	20.38 ± 0.01	-18.60	-19.57
169	141624.80+521625.2	0.2445	1	3.82	0.50	hi	18.31 ± 0.01	-20.72	-21.70
30	141749.15+523003.2	0.2462	1	1.48	0.44	hi	22.29 ± 0.03	-16.98	-17.72
163	141720.43+522251.5	0.2494	1	3.27	0.61	hi	19.52 ± 0.01	-19.61	-20.53
1088	141716.81+522406.8	0.25	2	1.95	0.19	li	18.44 ± 0.01	-20.52	-21.61
106	141623.32+521344.6	0.25	2	1.92	0.61	hi	21.07 ± 0.01	-17.75	-18.99
80	141737.46+522603.9	0.2589	1	1.69	0.39	hi	21.39 ± 0.03	-18.26	-18.73
75	141628.17+521630.1	0.2815	1	1.67	0.63	hi	19.91 ± 0.00	-19.30	-20.46
7	141654.73+521957.0	0.2816	1	1.41	0.51	hi	21.79 ± 0.03	-17.99	-18.54
1110	141721.71+522709.3	0.2819	1	2.18	0.27	li	19.15 ± 0.01	-20.72	-21.17
36	141525.37+520214.6	0.2822	1	1.50	0.61	hi	22.01 ± 0.02	-17.71	-18.33
152	141733.76+522520.1	0.285	2	2.59	0.47	hi	18.59 ± 0.01	-20.68	-21.82
1116	141641.21+522002.2	0.2877	1	2.32	0.17	li	19.98 ± 0.01	-19.58	-20.42
1006	141648.54+521914.6	0.305	2	1.41	0.16	li	20.23 ± 0.01	-19.52	-20.30
1119	141624.85+521351.3	0.325	2	2.38	0.33	li	20.00 ± 0.01	-19.82	-20.71
1054	141540.00+520743.8	0.33	2	1.61	0.23	li	21.24 ± 0.03	-18.57	-19.51
1141	141707.49+522148.0	0.3318	1	4.23	0.34	li	18.78 ± 0.02	-21.01	-22.00
88	141651.35+522052.3	0.3322	1	1.74	0.63	hi	21.20 ± 0.01	-18.79	-19.54
90	141650.08+521908.7	0.3335	1	1.75	0.39	hi	20.71 ± 0.02	-19.18	-20.05
1074	141641.98+521725.5	0.34	2	1.76	0.01	li	19.92 ± 0.02	-19.96	-20.91
61	141606.07+521233.8	0.3522	1	1.62	0.57	hi	19.38 ± 0.00	-20.29	-21.61
1047	141714.79+522150.5	0.3563	1	1.57	0.23	li	21.13 ± 0.02	-18.89	-19.82
128	141636.67+521739.9	0.357	1	2.13	0.38	hi	19.67 ± 0.02	-20.36	-21.29
108	141701.02+522114.2	0.365	2	1.95	0.63	hi	20.28 ± 0.01	-19.67	-20.78
1106	141613.66+521320.6	0.3656	1	2.10	0.12	li	19.88 ± 0.02	-20.26	-21.13
140	141739.02+522657.8	0.366	1	2.32	0.40	hi	21.02 ± 0.02	-19.38	-19.94
76	141642.31+521618.4	0.38	2	1.67	0.53	hi	20.77 ± 0.01	-19.14	-20.46
1055	141639.17+521608.9	0.385	2	1.61	0.26	li	20.69 ± 0.01	-19.65	-20.43
109	141624.71+521523.8	0.3929	1	1.95	0.39	hi	20.27 ± 0.02	-20.12	-20.92
141	141713.91+522550.6	0.4	2	2.33	0.39	hi	20.93 ± 0.02	-19.61	-20.27
1114	141653.57+522033.5	0.415	2	2.24	0.32	li	19.93 ± 0.01	-20.60	-21.41
70	141525.81+520545.3	0.4189	1	1.66	0.60	hi	20.57 ± 0.01	-20.05	-20.79
91	141657.48+521851.0	0.4193	1	1.76	0.45	hi	21.37 ± 0.02	-19.39	-19.92
15	141707.75+522153.5	0.4249	1	1.44	0.43	hi	21.46 ± 0.02	-19.30	-19.86
1100	141519.41+520359.1	0.4257	1	2.03	0.15	li	20.75 ± 0.02	-19.93	-20.61
1126	141726.43+522705.9	0.4261	1	2.46	0.07	li	19.18 ± 0.02	-21.47	-22.20
66	141646.12+521753.6	0.4323	1	1.63	0.39	hi	20.92 ± 0.01	-19.87	-20.46
1042	141747.21+523141.0	0.435	2	1.55	0.09	li	20.98 ± 0.02	-19.67	-20.46
1136	141639.56+521614.6	0.4402	1	3.00	0.17	li	19.98 ± 0.02	-20.64	-21.53
1029	141703.29+521934.3	0.445	2	1.50	0.35	li	20.53 ± 0.01	-20.09	-21.04
1133	141530.17+520511.1	0.4499	1	2.65	0.23	li	19.98 ± 0.02	-20.69	-21.59
17	141723.09+522517.4	0.4636	1	1.44	0.54	hi	21.54 ± 0.02	-19.29	-20.07
1103	141628.07+521457.5	0.47	2	2.08	0.08	li	20.39 ± 0.02	-20.34	-21.35
117	141609.78+521211.2	0.4715	1	2.02	0.53	hi	20.24 ± 0.01	-20.49	-21.54

Table A.2. Continued.

No. (1)	Source ID (2)	z (3)	Qz (4)	R (arcsec) (5)	ϵ (6)	Sample (7)	I_{814} (8)	M_B (9)	M_R (10)
125	141619.45+521154.9	0.475	2	2.09	0.64	hi	21.17 ± 0.02	-19.82	-20.47
113	141654.57+521858.1	0.4757	1	1.96	0.54	hi	21.07 ± 0.02	-19.83	-20.62
1043	141607.85+521226.4	0.48	2	1.55	0.32	li	20.86 ± 0.01	-20.13	-20.81
34	141518.75+520158.6	0.485	1	1.49	0.40	hi	21.94 ± 0.03	-19.13	-19.70
112	141717.42+522330.4	0.49	2	1.96	0.38	hi	20.80 ± 0.02	-20.20	-20.94
64	141644.02+521630.7	0.5076	1	1.63	0.56	hi	20.91 ± 0.01	-20.01	-21.05
1107	141608.60+521041.6	0.51	2	2.10	0.09	li	20.20 ± 0.01	-20.78	-21.76
42	141611.95+521002.2	0.515	2	1.52	0.51	hi	21.02 ± 0.01	-20.13	-20.82
69	141549.44+520755.6	0.515	2	1.64	0.62	hi	21.38 ± 0.02	-19.47	-20.72
1121	141612.66+521337.0	0.52	2	2.43	0.15	li	20.80 ± 0.02	-20.49	-20.97
1044	141731.75+522605.4	0.534	1	1.56	0.22	li	21.38 ± 0.03	-19.97	-20.45
32	141715.80+522249.3	0.5341	1	1.48	0.56	hi	21.18 ± 0.01	-19.96	-20.92
1037	141528.33+520420.2	0.54	2	1.53	0.28	li	20.76 ± 0.01	-20.38	-21.37
3	141713.40+522145.3	0.5486	1	1.40	0.53	hi	21.60 ± 0.02	-19.61	-20.52
105	141557.80+520914.0	0.55	2	1.91	0.66	hi	21.48 ± 0.02	-19.61	-20.84
23	141552.30+520951.1	0.56	2	1.46	0.48	hi	21.65 ± 0.02	-19.82	-20.29
1053	141543.90+520925.6	0.565	2	1.60	0.16	li	20.80 ± 0.01	-20.57	-21.36
158	141537.47+520537.5	0.5724	1	2.87	0.56	hi	20.25 ± 0.02	-20.92	-22.17
49	141553.02+520850.7	0.595	2	1.55	0.40	hi	21.43 ± 0.03	-19.79	-21.22
11	141700.45+522241.8	0.605	2	1.42	0.47	hi	21.37 ± 0.02	-20.13	-20.99
149	141536.16+520441.9	0.6068	1	2.55	0.66	hi	20.53 ± 0.01	-20.79	-22.15
136	141721.04+522316.4	0.6143	1	2.23	0.50	hi	20.28 ± 0.01	-21.15	-22.34
46	141644.24+521718.5	0.615	2	1.54	0.47	hi	21.51 ± 0.02	-19.88	-21.22
146	141523.88+520322.2	0.6227	1	2.46	0.48	hi	21.56 ± 0.04	-20.20	-20.54
1016	141618.38+521335.2	0.6404	1	1.46	0.24	li	20.45 ± 0.01	-21.08	-22.27
1123	141615.73+521342.8	0.6418	1	2.44	0.12	li	20.15 ± 0.02	-21.50	-22.42
1102	141550.99+521004.3	0.645	2	2.06	0.17	li	20.33 ± 0.01	-21.49	-21.95
1031	141535.54+520703.1	0.6495	1	1.50	0.37	li	21.86 ± 0.03	-19.93	-20.50
1090	141534.53+520700.7	0.6496	1	1.96	0.25	li	20.37 ± 0.01	-21.33	-22.28
94	141511.76+520219.5	0.6597	1	1.80	0.66	hi	21.53 ± 0.02	-20.04	-21.59
132	141648.32+521938.7	0.6736	1	2.17	0.57	hi	21.49 ± 0.03	-20.41	-21.02
84	141630.53+521538.3	0.6838	1	1.71	0.41	hi	21.50 ± 0.03	-20.38	-21.20
74	141621.55+521331.8	0.6838	1	1.67	0.60	hi	21.81 ± 0.02	-20.09	-20.88
20	141617.62+521349.4	0.6848	1	1.45	0.47	hi	22.08 ± 0.04	-19.85	-20.43
40	141639.04+521648.2	0.72	2	1.51	0.54	hi	22.06 ± 0.04	-19.96	-20.84
96	141635.26+521740.3	0.7507	1	1.82	0.65	hi	21.86 ± 0.03	-20.26	-21.48
1127	141626.07+521601.8	0.7507	1	2.48	0.25	li	21.17 ± 0.04	-20.99	-21.72
1009	141740.54+522713.5	0.754	1	1.41	0.11	li	20.55 ± 0.01	-21.61	-22.50
156	141739.86+522821.4	0.7553	1	2.80	0.59	hi	20.68 ± 0.02	-21.48	-22.56
1082	141656.55+522007.9	0.76	2	1.83	0.25	li	20.74 ± 0.02	-21.42	-22.61
126	141617.03+521433.8	0.805	2	2.09	0.43	hi	21.17 ± 0.03	-21.22	-22.57
65	141536.52+520421.6	0.812	1	1.63	0.50	hi	21.72 ± 0.03	-20.67	-21.14
39	141617.69+521453.7	0.813	1	1.51	0.60	hi	22.15 ± 0.04	-20.26	-21.32
1095	141531.40+520456.0	0.825	2	2.01	0.17	li	21.55 ± 0.04	-20.89	-21.64
1084	141518.71+520321.3	0.8712	1	1.86	0.33	li	21.31 ± 0.04	-21.33	-22.23
55	141754.08+522911.3	0.8782	1	1.58	0.51	hi	22.06 ± 0.03	-20.54	-20.98
1019	141649.12+521806.0	0.895	2	1.47	0.28	li	21.47 ± 0.02	-21.30	-22.23
1079	141651.22+521813.0	0.9325	1	1.81	0.26	li	21.10 ± 0.02	-21.82	-22.63
57	141535.41+520727.8	0.935	2	1.59	0.51	hi	21.83 ± 0.03	-21.23	-22.50
1023	141721.38+522610.8	0.945	2	1.48	0.11	li	22.12 ± 0.06	-20.87	-21.87
1064	141800.64+523234.6	0.969	1	1.69	0.36	li	21.66 ± 0.03	-21.33	-22.07
1021	141742.82+522948.5	0.985	2	1.47	0.34	li	22.34 ± 0.06	-20.86	-21.94
1004	141733.84+522724.7	0.9877	1	1.40	0.28	li	21.43 ± 0.02	-21.76	-22.57
1062	141727.30+522500.8	0.99	1	1.65	0.22	li	21.51 ± 0.03	-21.56	-22.19
14	141732.48+522549.2	0.9962	1	1.44	0.64	hi	22.60 ± 0.05	-20.56	-21.35
58	141609.79+521409.0	1.0015	1	1.60	0.61	hi	21.73 ± 0.03	-21.57	-22.41
26	141727.82+522421.9	1.01	2	1.47	0.60	hi	22.23 ± 0.03	-21.00	-21.49
16	141631.78+521728.1	1.0287	1	1.44	0.64	hi	22.60 ± 0.04	-20.75	-21.64
1091	141547.16+520847.2	1.04	2	1.98	0.16	li	21.54 ± 0.03	-21.79	-22.50
1001	141607.76+521059.3	1.08	2	1.40	0.09	li	22.00 ± 0.05	-21.38	-21.83
114	141716.86+522508.1	1.085	2	2.00	0.48	hi	21.99 ± 0.04	-21.47	-22.09
1045	141545.61+520654.9	1.085	2	1.56	0.10	li	21.97 ± 0.05	-21.49	-22.26
1092	141608.94+521033.3	1.095	2	1.99	0.17	li	21.30 ± 0.03	-22.43	-23.55
19	141803.98+523218.9	1.105	2	1.45	0.48	hi	22.09 ± 0.04	-21.40	-21.93
85	141554.65+521050.6	1.1203	1	1.72	0.39	hi	21.70 ± 0.04	-21.93	-22.70
21	141706.80+522256.5	1.13	2	1.46	0.50	hi	22.30 ± 0.06	-21.55	-22.60

Table A.2. Continued.

No. (1)	Source ID (2)	z (3)	Qz (4)	R (arcsec) (5)	ϵ (6)	Sample (7)	I_{814} (8)	M_B (9)	M_R (10)
122	141609.95+521008.8	1.135	2	2.05	0.63	hi	21.87 ± 0.04	-21.95	-22.68
73	141640.24+521829.1	1.145	2	1.67	0.38	hi	21.88 ± 0.03	-21.82	-22.22
1067	141638.99+521702.4	1.185	2	1.70	0.36	li	22.08 ± 0.04	-21.70	-22.30
1003	141531.13+520657.1	1.2	2	1.40	0.13	li	21.87 ± 0.03	-22.29	-23.13
147	141709.81+522114.4	1.2304	1	2.49	0.62	hi	21.93 ± 0.04	-22.08	-22.78

Table A.3. Bulge sample colours

No. (1)	$(V_{606} - I_{814})_b$ (2)	$(V_{606} - I_{814})_d$ (3)	$(V_{606} - I_{814})_g$ (4)	$(U - B)_b$ (5)	$(U - B)_d$ (6)	$(U - B)_g$ (7)	$(B - R)_b$ (8)	$(B - R)_d$ (9)	$(B - R)_g$ (10)
1131	0.67 ± 0.33	0.75 ± 0.03	0.64 ± 0.00	-0.13	-0.06	-0.17	0.79	0.87	0.76
1139	0.92 ± 0.20	0.95 ± 0.05	0.93 ± 0.00	0.42	0.45	0.43	1.37	1.40	1.38
1078	0.76 ± 0.12	0.86 ± 0.04	0.81 ± 0.01	0.08	0.18	0.14	1.03	1.13	1.08
1081	1.08 ± 0.26	1.03 ± 0.18	1.06 ± 0.00	0.54	0.49	0.52	1.49	1.45	1.47
1125	1.00 ± 0.45	1.00 ± 0.11	1.08 ± 0.01	0.27	0.27	0.35	1.34	1.34	1.41
139	0.82 ± 0.26	0.74 ± 1.27	0.91 ± 0.02	0.05	-0.04	0.14	1.01	0.92	1.10
170	0.95 ± 0.13	0.66 ± 0.15	0.79 ± 0.01	0.12	-0.17	-0.04	1.05	0.77	0.90
159	1.16 ± 0.06	1.09 ± 0.11	1.16 ± 0.00	0.41	0.33	0.41	1.41	1.34	1.41
1005	0.87 ± 0.14	0.97 ± 0.62	1.10 ± 0.01	0.11	0.21	0.34	1.09	1.19	1.31
1099	1.04 ± 0.04	1.17 ± 0.04	1.13 ± 0.01	0.54	0.67	0.63	1.21	1.33	1.29
47	1.01 ± 0.02	1.31 ± 0.09	1.31 ± 0.01	0.38	0.69	0.68	1.27	1.58	1.57
1138	1.11 ± 0.13	1.22 ± 0.09	1.27 ± 0.00	0.43	0.54	0.60	1.36	1.47	1.52
1063	0.92 ± 0.03	1.08 ± 0.03	1.08 ± 0.01	0.11	0.27	0.27	1.05	1.22	1.22
1020	0.84 ± 0.03	0.84 ± 0.03	0.79 ± 0.01	0.03	0.03	-0.01	0.82	0.82	0.78
1135	0.90 ± 0.04	1.16 ± 0.08	1.08 ± 0.01	-0.01	0.25	0.17	0.98	1.24	1.15
1137	1.28 ± 0.10	1.26 ± 0.06	1.33 ± 0.00	0.52	0.50	0.57	1.40	1.38	1.45
1118	0.79 ± 0.07	0.67 ± 0.09	0.78 ± 0.01	-0.14	-0.25	-0.14	0.78	0.66	0.77
1142	1.26 ± 0.07	0.87 ± 0.25	1.13 ± 0.01	0.28	-0.11	0.15	1.31	0.93	1.19
104	1.41 ± 0.04	1.27 ± 0.19	1.37 ± 0.01	0.45	0.31	0.42	1.46	1.32	1.42
1108	1.50 ± 0.07	1.37 ± 0.12	1.43 ± 0.01	0.53	0.40	0.46	1.50	1.37	1.43
1057	1.16 ± 0.09	1.37 ± 0.05	1.34 ± 0.01	0.29	0.51	0.47	1.11	1.33	1.29
1046	1.35 ± 0.05	1.41 ± 0.24	1.41 ± 0.01	0.40	0.46	0.46	1.29	1.35	1.35
155	1.60 ± 0.01	1.38 ± 0.30	1.44 ± 0.01	0.54	0.33	0.39	1.59	1.38	1.44
1024	1.12 ± 0.00	1.16 ± 0.38	1.03 ± 0.01	0.09	0.13	0.01	1.04	1.08	0.95
1068	1.37 ± 0.01	1.10 ± 0.13	1.12 ± 0.01	0.32	0.05	0.07	1.32	1.05	1.07
123	1.19 ± 0.01	0.93 ± 0.07	1.04 ± 0.01	0.15	-0.10	0.00	1.11	0.85	0.96
1093	0.66 ± 0.00	1.08 ± 0.19	1.02 ± 0.01	-0.41	0.01	-0.04	0.55	0.97	0.91
134	1.65 ± 0.01	1.44 ± 0.17	1.52 ± 0.01	0.76	0.56	0.64	1.43	1.22	1.30
1077	1.51 ± 0.01	1.32 ± 0.32	1.54 ± 0.02	0.33	0.14	0.36	1.33	1.14	1.36
1122	1.36 ± 0.02	1.22 ± 0.10	1.26 ± 0.01	0.24	0.11	0.14	1.24	1.10	1.14
1033	1.51 ± 0.00	1.45 ± 0.16	1.54 ± 0.02	0.46	0.40	0.49	1.32	1.27	1.36
1117	1.65 ± 0.00	1.61 ± 0.14	1.58 ± 0.01	0.57	0.52	0.50	1.46	1.41	1.38
110	0.70 ± 0.00	1.08 ± 0.08	1.00 ± 0.01	-0.31	0.06	-0.01	0.52	0.89	0.82
162	1.58 ± 0.02	1.07 ± 0.33	1.23 ± 0.02	0.43	-0.08	0.08	1.48	0.97	1.13
102	1.22 ± 0.00	1.41 ± 0.10	1.46 ± 0.01	0.00	0.19	0.24	0.88	1.07	1.12
1017	1.16 ± 0.00	1.20 ± 0.14	1.27 ± 0.02	-0.08	-0.04	0.02	0.91	0.95	1.02
116	1.83 ± 0.03	1.41 ± 0.49	1.66 ± 0.03	0.48	0.05	0.31	1.45	1.03	1.28
1113	1.77 ± 0.00	1.66 ± 0.12	1.64 ± 0.01	0.39	0.28	0.25	1.31	1.20	1.18
1083	1.70 ± 0.00	1.79 ± 0.11	1.83 ± 0.01	0.30	0.38	0.42	1.27	1.36	1.40
1115	1.61 ± 0.01	1.37 ± 0.19	1.40 ± 0.01	0.27	0.03	0.06	1.30	1.06	1.09
142	1.01 ± 0.00	1.64 ± 0.25	1.32 ± 0.01	-0.27	0.36	0.04	0.74	1.37	1.05
1036	1.40 ± 0.03	1.08 ± 0.25	1.15 ± 0.02	0.16	-0.17	-0.10	0.98	0.65	0.73
1028	1.63 ± 0.04	1.06 ± 0.35	1.38 ± 0.03	0.27	-0.30	0.03	1.25	0.68	1.00
150	2.17 ± 0.06	1.68 ± 1.29	1.87 ± 0.03	0.66	0.17	0.36	1.66	1.18	1.37
1034	1.91 ± 0.01	1.76 ± 0.13	1.88 ± 0.02	0.38	0.23	0.35	1.15	1.01	1.12
1048	1.61 ± 0.02	1.47 ± 0.15	1.58 ± 0.02	0.12	-0.02	0.10	1.06	0.92	1.03
8	2.09 ± 0.03	1.47 ± 0.98	1.95 ± 0.05	0.53	-0.08	0.39	1.54	0.92	1.39
160	1.97 ± 0.01	1.80 ± 0.25	1.95 ± 0.02	0.37	0.19	0.34	1.15	0.97	1.12
1065	2.07 ± 0.01	2.17 ± 0.64	2.13 ± 0.02	0.43	0.54	0.49	1.38	1.49	1.45
1035	2.09 ± 0.01	1.92 ± 0.22	1.99 ± 0.02	0.52	0.35	0.42	1.42	1.25	1.33
129	1.86 ± 0.05	1.31 ± 0.32	1.64 ± 0.04	0.36	-0.19	0.14	1.30	0.76	1.09
1097	1.56 ± 0.05	1.35 ± 0.64	1.35 ± 0.03	0.08	-0.12	-0.13	0.86	0.66	0.65
59	2.07 ± 0.05	1.62 ± 0.30	1.84 ± 0.05	0.53	0.07	0.29	1.46	1.01	1.23
1	0.90 ± 0.08 ±	1.14 ± 0.10	-0.26	-0.02	0.67	0.91

Table A.4. Non-bulge sample colours

No. (1)	$(V_{606} - I_{814})_b$ (2)	$(V_{606} - I_{814})_d$ (3)	$(V_{606} - I_{814})_g$ (4)	$(U - B)_b$ (5)	$(U - B)_d$ (6)	$(U - B)_g$ (7)	$(B - R)_b$ (8)	$(B - R)_d$ (9)	$(B - R)_g$ (10)
86	0.75 ± 3.76	0.78 ± 0.10	0.67 ± 0.02	-0.05	-0.01	-0.12	0.90	0.93	0.82
1098	0.83 ± 0.18	0.77 ± 0.03	0.70 ± 0.00	0.00	-0.05	-0.13	0.99	0.93	0.86
133	0.50 ± 0.53	0.75 ± 0.06	0.74 ± 0.02	0.13	0.38	0.37	0.81	1.06	1.05
164	0.76 ± 0.33	0.79 ± 0.24	0.63 ± 0.02	0.07	0.10	-0.06	0.86	0.89	0.74
165	0.72 ± 0.23	0.75 ± 0.06	0.74 ± 0.01	0.08	0.11	0.10	0.98	1.01	1.00
138	0.71 ± 0.43	0.69 ± 0.19	0.51 ± 0.02	0.06	0.05	-0.13	0.77	0.75	0.57
131	0.70 ± 0.11	0.73 ± 0.05	0.71 ± 0.01	0.08	0.10	0.08	0.91	0.93	0.92
148	0.97 ± 0.33	0.71 ± 0.25	0.63 ± 0.02	0.36	0.10	0.01	1.08	0.83	0.74
1025	0.38 ± 0.63	0.94 ± 0.78	0.58 ± 0.06	0.08	0.63	0.28	0.53	1.09	0.73
9	0.49 ± 0.67	0.68 ± 0.31	0.61 ± 0.05	-0.14	0.04	-0.03	0.62	0.80	0.73
43	0.71 ± 0.37	0.68 ± 0.17	0.62 ± 0.05	0.05	0.02	-0.05	0.88	0.86	0.79
157	0.75 ± 0.04	0.75 ± 0.08	0.77 ± 0.01	0.07	0.06	0.08	0.91	0.90	0.93
137	0.97 ± 0.21	0.66 ± 0.09	0.62 ± 0.02	0.28	-0.02	-0.06	1.07	0.76	0.73
166	0.60 ± 0.11	0.63 ± 0.10	0.67 ± 0.01	-0.18	-0.15	-0.11	0.67	0.70	0.75
154	0.84 ± 0.18	0.86 ± 0.05	0.90 ± 0.01	0.13	0.15	0.19	1.07	1.09	1.12
48	0.56 ± 0.42	0.57 ± 0.19	0.57 ± 0.06	-0.11	-0.11	-0.10	0.62	0.63	0.63
1061	0.85 ± 0.17	0.77 ± 0.05	0.80 ± 0.01	0.08	0.00	0.03	0.97	0.89	0.92
1134	0.82 ± 0.19	0.88 ± 0.10	0.87 ± 0.01	0.07	0.14	0.13	1.03	1.09	1.08
1076	0.83 ± 0.04	0.81 ± 0.03	0.80 ± 0.02	0.14	0.12	0.11	0.98	0.96	0.95
1066	0.75 ± 0.18	0.69 ± 0.16	0.76 ± 0.02	0.01	-0.04	0.03	0.85	0.80	0.87
93	0.67 ± 0.11	0.72 ± 0.10	0.80 ± 0.03	-0.13	-0.08	0.00	0.79	0.84	0.92
1039	0.65 ± 0.18	0.82 ± 0.28	0.66 ± 0.05	-0.22	-0.06	-0.22	0.72	0.88	0.72
1094	0.90 ± 0.10	0.93 ± 0.04	0.86 ± 0.01	0.15	0.19	0.12	1.06	1.09	1.02
169	1.09 ± 0.08	0.83 ± 0.06	0.92 ± 0.00	0.19	-0.06	0.02	1.24	0.98	1.07
30	0.69 ± 0.10	0.62 ± 0.13	0.63 ± 0.05	-0.09	-0.17	-0.16	0.77	0.69	0.70
163	0.93 ± 0.09	0.72 ± 0.15	0.84 ± 0.01	0.06	-0.15	-0.03	1.07	0.86	0.97
1088	1.04 ± 0.01	0.90 ± 0.02	0.97 ± 0.00	0.20	0.06	0.13	1.22	1.08	1.15
106	0.92 ± 0.24	1.02 ± 0.06	0.99 ± 0.02	0.17	0.27	0.25	1.15	1.25	1.23
80	0.61 ± 0.14	0.45 ± 0.11	0.53 ± 0.02	-0.06	-0.22	-0.14	0.61	0.45	0.53
75	1.00 ± 0.12	0.90 ± 0.10	1.02 ± 0.01	0.15	0.05	0.17	1.17	1.07	1.18
7	0.52 ± 0.17	0.68 ± 0.09	0.65 ± 0.03	-0.19	-0.04	-0.06	0.52	0.68	0.65
1110	0.60 ± 0.01	0.66 ± 0.03	0.55 ± 0.01	-0.17	-0.12	-0.22	0.58	0.64	0.53
36	0.51 ± 0.07	0.75 ± 0.20	0.63 ± 0.04	-0.22	0.02	-0.10	0.53	0.77	0.65
152	1.07 ± 0.03	0.96 ± 0.04	1.02 ± 0.00	0.18	0.06	0.13	1.23	1.11	1.18
1116	0.84 ± 0.07	1.46 ± 1.92	0.82 ± 0.01	-0.07	0.54	-0.10	0.92	1.53	0.90
1006	0.78 ± 0.07	0.76 ± 0.02	0.83 ± 0.01	-0.01	-0.03	0.03	0.83	0.81	0.88
1119	0.91 ± 0.08	0.90 ± 0.06	0.86 ± 0.01	0.09	0.07	0.03	0.97	0.96	0.91
1054	0.98 ± 0.10	0.91 ± 0.12	0.94 ± 0.03	0.11	0.04	0.07	1.04	0.97	1.01
1141	1.06 ± 0.07	0.91 ± 0.14	0.91 ± 0.01	0.18	0.03	0.03	1.14	0.99	0.99
88	0.83 ± 0.17	0.78 ± 0.08	0.78 ± 0.02	0.04	-0.02	-0.01	0.84	0.79	0.79
90	0.85 ± 0.08	0.86 ± 0.06	0.84 ± 0.02	0.17	0.19	0.16	0.88	0.89	0.87
1074	1.00 ± 0.05	0.93 ± 0.07	0.93 ± 0.01	0.11	0.03	0.03	1.06	0.98	0.98
61	1.22 ± 0.10	1.24 ± 0.02	1.24 ± 0.01	0.53	0.55	0.55	1.36	1.37	1.37
1047	0.85 ± 0.17	1.05 ± 0.08	0.89 ± 0.02	-0.05	0.15	0.00	0.88	1.08	0.92
128	0.98 ± 0.03	0.93 ± 0.06	0.80 ± 0.01	0.08	0.03	0.00	1.01	0.96	0.93
108	1.05 ± 0.05	1.13 ± 0.04	1.05 ± 0.01	0.15	0.23	0.14	1.11	1.20	1.11
1106	1.09 ± 0.04	0.85 ± 0.06	0.91 ± 0.01	0.22	-0.02	0.05	1.10	0.86	0.92
140	0.89 ± 0.14	0.89 ± 0.23	0.74 ± 0.02	0.13	0.14	-0.01	0.83	0.83	0.69
76	1.34 ± 0.08	1.28 ± 0.45	1.24 ± 0.02	0.38	0.31	0.27	1.45	1.39	1.35
1055	0.86 ± 0.13	0.79 ± 0.06	0.82 ± 0.02	-0.08	-0.16	-0.13	0.85	0.77	0.80
109	0.85 ± 0.09	0.74 ± 0.08	0.83 ± 0.01	-0.02	-0.13	-0.04	0.82	0.71	0.80
141	0.93 ± 0.05	0.73 ± 0.16	0.74 ± 0.02	0.07	-0.13	-0.12	0.86	0.66	0.68
1114	1.08 ± 0.07	0.81 ± 0.03	0.84 ± 0.01	0.13	-0.14	-0.11	1.04	0.78	0.81
70	0.89 ± 0.25	0.90 ± 0.03	0.91 ± 0.01	0.12	0.12	0.13	0.82	0.82	0.83
91	0.70 ± 0.08	0.65 ± 0.12	0.69 ± 0.03	-0.16	-0.21	-0.18	0.60	0.55	0.59
15	0.58 ± 0.08	0.70 ± 0.08	0.68 ± 0.03	-0.31	-0.19	-0.21	0.47	0.59	0.57
1100	0.79 ± 0.16	0.93 ± 0.19	0.82 ± 0.02	-0.09	0.05	-0.07	0.71	0.84	0.73
1126	0.90 ± 0.05	0.91 ± 0.07	0.85 ± 0.01	0.00	0.00	-0.05	0.82	0.82	0.77
66	0.73 ± 0.02	0.73 ± 0.07	0.74 ± 0.02	-0.14	-0.14	-0.13	0.62	0.62	0.63
1042	1.13 ± 0.11	0.88 ± 0.08	0.95 ± 0.02	0.21	-0.04	0.03	1.05	0.80	0.87
1136	1.01 ± 0.10	0.75 ± 0.25	0.93 ± 0.01	0.01	-0.24	-0.06	0.96	0.71	0.89
1029	1.13 ± 0.05	1.15 ± 0.06	1.05 ± 0.02	0.17	0.19	0.09	1.08	1.10	1.00
1133	1.22 ± 0.07	1.03 ± 0.08	0.99 ± 0.01	0.27	0.09	0.05	1.14	0.95	0.91
17	0.89 ± 0.10	0.96 ± 0.05	0.94 ± 0.03	-0.07	0.00	-0.02	0.78	0.85	0.82
1103	1.19 ± 0.03	1.15 ± 0.16	1.12 ± 0.02	0.15	0.12	0.08	1.11	1.08	1.04
117	1.29 ± 0.02	0.58 ± 2.58	1.06 ± 0.01	0.26	-0.44	0.04	1.25	0.54	1.03

Table A.4. Continued.

No. (1)	$(V_{606} - I_{814})_b$ (2)	$(V_{606} - I_{814})_d$ (3)	$(V_{606} - I_{814})_g$ (4)	$(U - B)_b$ (5)	$(U - B)_d$ (6)	$(U - B)_g$ (7)	$(B - R)_b$ (8)	$(B - R)_d$ (9)	$(B - R)_g$ (10)
125	0.93 ± 0.03	0.90 ± 0.15	0.86 ± 0.02	0.09	0.06	0.02	0.76	0.73	0.69
113	1.17 ± 0.03	0.74 ± 1.01	0.91 ± 0.02	0.16	-0.27	-0.10	1.07	0.64	0.81
1043	0.82 ± 0.02	0.84 ± 0.01	0.80 ± 0.02	-0.20	-0.18	-0.22	0.70	0.72	0.68
34	0.82 ± 0.04	0.73 ± 0.16	0.77 ± 0.04	-0.13	-0.22	-0.18	0.64	0.55	0.59
112	0.97 ± 0.03	0.86 ± 0.07	0.96 ± 0.02	-0.01	-0.12	-0.02	0.80	0.69	0.80
64	1.05 ± 0.02	1.07 ± 0.13	1.11 ± 0.02	-0.02	-0.01	0.03	0.91	0.93	0.97
1107	1.27 ± 0.03	1.12 ± 0.25	1.14 ± 0.02	0.18	0.03	0.05	1.16	1.01	1.02
42	1.01 ± 0.02	0.90 ± 0.06	0.94 ± 0.02	0.01	-0.10	-0.07	0.80	0.69	0.73
69	1.48 ± 0.04	1.14 ± 0.32	1.34 ± 0.03	0.36	0.02	0.21	1.38	1.04	1.23
1121	0.94 ± 0.04	0.95 ± 0.13	0.83 ± 0.03	0.06	0.07	-0.05	0.64	0.64	0.53
1044	0.84 ± 0.04	0.93 ± 0.07	0.88 ± 0.03	-0.08	0.01	-0.05	0.54	0.63	0.58
32	1.00 ± 0.02	1.02 ± 0.09	1.05 ± 0.02	-0.10	-0.08	-0.06	0.87	0.89	0.91
1037	1.43 ± 0.03	1.35 ± 0.08	1.30 ± 0.02	0.33	0.25	0.20	1.26	1.18	1.13
3	1.09 ± 0.03	1.15 ± 0.13	1.11 ± 0.03	-0.05	0.01	-0.02	0.88	0.94	0.91
105	1.54 ± 0.06	1.02 ± 0.35	1.27 ± 0.04	0.36	-0.16	0.08	1.42	0.90	1.15
23	0.92 ± 0.04	0.90 ± 0.81	0.88 ± 0.03	-0.06	-0.08	-0.10	0.58	0.56	0.54
1053	1.09 ± 0.03	1.05 ± 0.08	1.03 ± 0.02	0.03	-0.01	-0.03	0.85	0.82	0.80
158	1.47 ± 0.04	1.32 ± 0.20	1.43 ± 0.02	0.26	0.10	0.21	1.24	1.08	1.19
49	1.41 ± 0.05	1.72 ± 0.20	1.63 ± 0.04	0.14	0.44	0.36	1.14	1.45	1.36
11	1.02 ± 0.03	1.16 ± 2.11	1.10 ± 0.03	-0.19	-0.04	-0.11	0.74	0.88	0.81
149	1.62 ± 0.01	1.51 ± 0.08	1.71 ± 0.02	0.31	0.20	0.40	1.33	1.23	1.43
136	1.58 ± 0.02	1.37 ± 0.07	1.29 ± 0.02	0.31	0.09	0.02	1.30	1.09	1.01
46	1.28 ± 0.03	1.42 ± 0.11	1.35 ± 0.04	-0.03	0.12	0.04	1.04	1.18	1.11
146	1.14 ± 0.10	0.94 ± 0.21	0.97 ± 0.05	0.13	-0.07	-0.04	0.56	0.36	0.39
1016	1.78 ± 0.01	1.74 ± 0.08	1.70 ± 0.02	0.49	0.46	0.41	1.27	1.23	1.18
1123	1.51 ± 0.04	1.27 ± 0.26	1.25 ± 0.02	0.22	-0.02	-0.04	1.14	0.90	0.88
1102	0.99 ± 0.02	0.93 ± 0.11	0.91 ± 0.01	-0.18	-0.23	-0.26	0.55	0.50	0.47
1031	1.26 ± 0.07	1.10 ± 0.20	1.05 ± 0.04	0.12	-0.03	-0.09	0.82	0.66	0.61
1090	1.53 ± 0.02	1.30 ± 0.20	1.26 ± 0.02	0.23	0.00	-0.04	1.22	1.00	0.95
94	1.81 ± 0.05	1.91 ± 0.18	1.78 ± 0.05	0.40	0.50	0.37	1.50	1.61	1.48
132	1.31 ± 0.06	0.95 ± 0.30	1.04 ± 0.03	0.10	-0.26	-0.17	0.90	0.54	0.63
84	1.29 ± 0.05	1.34 ± 0.84	1.46 ± 0.04	0.06	0.10	0.23	0.67	0.72	0.84
74	1.33 ± 0.06	1.18 ± 0.50	1.34 ± 0.05	0.02	-0.13	0.04	0.86	0.71	0.87
20	1.14 ± 0.08	0.91 ± 0.19	0.96 ± 0.05	-0.11	-0.34	-0.29	0.69	0.46	0.51
40	1.42 ± 0.09	1.47 ± 0.25	1.25 ± 0.06	0.08	0.14	-0.08	1.01	1.06	0.84
96	1.18 ± 0.07	1.41 ± 0.44	1.55 ± 0.06	-0.30	-0.07	0.07	0.69	0.92	1.06
1127	1.50 ± 0.06	1.20 ± 0.35	1.32 ± 0.04	0.17	-0.13	-0.01	0.94	0.64	0.76
1009	1.21 ± 0.01	1.28 ± 0.12	1.47 ± 0.02	-0.25	-0.17	0.01	0.45	0.52	0.71
156	1.99 ± 0.05	1.45 ± 0.15	1.49 ± 0.03	0.57	0.03	0.07	1.54	1.00	1.04
1082	1.80 ± 0.03	1.48 ± 0.10	1.44 ± 0.02	0.34	0.02	-0.02	1.34	1.02	0.98
126	1.72 ± 0.04	1.81 ± 0.29	1.55 ± 0.04	0.23	0.32	0.05	1.28	1.37	1.10
65	1.26 ± 0.07	1.15 ± 0.45	1.20 ± 0.04	-0.17	-0.29	-0.24	0.51	0.40	0.45
39	1.48 ± 0.08	1.25 ± 0.17	1.36 ± 0.06	0.10	-0.13	-0.02	1.08	0.86	0.97
1095	0.91 ± 0.13	0.64 ± 1.56	1.00 ± 0.04	-0.48	-0.75	-0.39	0.59	0.32	0.68
1084	1.70 ± 0.06	1.52 ± 0.30	1.46 ± 0.04	0.19	0.01	-0.05	1.12	0.94	0.88
55	1.22 ± 0.07	0.91 ± 0.30	1.07 ± 0.05	-0.22	-0.54	-0.38	0.53	0.22	0.38
1019	1.66 ± 0.04	1.21 ± 0.13	1.38 ± 0.04	0.17	-0.28	-0.11	1.08	0.63	0.80
1079	1.62 ± 0.06	1.26 ± 0.23	1.37 ± 0.03	0.15	-0.21	-0.11	0.92	0.56	0.67
57	2.04 ± 0.12	1.69 ± 0.34	1.82 ± 0.06	0.50	0.14	0.27	1.44	1.08	1.21
1023	1.38 ± 0.09	1.84 ± 2.27	1.26 ± 0.06	0.02	0.48	-0.10	1.01	1.47	0.89
1064	0.75 ± 0.06	0.77 ± 0.11	0.71 ± 0.03	-0.48	-0.46	-0.52	0.53	0.55	0.49
1021	1.64 ± 0.17	0.94 ± 0.37	1.39 ± 0.08	0.33	-0.37	0.08	1.32	0.61	1.06
1004	0.85 ± 0.04	1.33 ± 0.33	1.45 ± 0.04	-0.65	-0.17	-0.06	0.05	0.52	0.64
1062	1.09 ± 0.05	1.06 ± 0.20	1.16 ± 0.04	-0.29	-0.33	-0.23	0.57	0.54	0.63
14	1.49 ± 0.09	0.90 ± 0.19	1.46 ± 0.09	-0.04	-0.62	-0.07	0.80	0.22	0.77
58	1.44 ± 0.04	1.41 ± 0.14	1.57 ± 0.05	0.09	0.05	0.22	0.72	0.69	0.85
26	1.26 ± 0.05	1.17 ± 0.13	1.44 ± 0.07	-0.21	-0.30	-0.03	0.29	0.20	0.47
16	1.27 ± 0.10	1.35 ± 0.12	1.21 ± 0.08	0.03	0.10	-0.04	0.93	1.00	0.86
1091	0.65 ± 0.06	1.33 ± 0.31	1.00 ± 0.04	-0.52	0.16	-0.17	0.31	0.99	0.67
1001	1.13 ± 0.09	0.82 ± 0.17	0.91 ± 0.05	-0.08	-0.40	-0.31	0.64	0.32	0.41
114	1.02 ± 0.06	1.20 ± 0.26	1.03 ± 0.05	-0.25	-0.06	-0.23	0.55	0.73	0.56
1045	1.63 ± 0.14	1.31 ± 1.30	1.12 ± 0.06	0.30	-0.02	-0.21	1.26	0.95	0.76
1092	1.89 ± 0.08	1.74 ± 0.20	1.30 ± 0.04	0.66	0.51	0.07	1.63	1.48	1.04
19	1.24 ± 0.08	1.08 ± 0.13	0.99 ± 0.05	0.01	-0.14	-0.24	0.77	0.62	0.52
85	1.03 ± 0.14	1.03 ± 0.17	1.17 ± 0.04	-0.32	-0.32	-0.18	0.59	0.58	0.72
21	1.12 ± 0.16	0.48 ± 0.49	1.22 ± 0.08	-0.06	-0.70	0.05	0.88	0.24	0.98

Table A.4. Continued.

No. (1)	$(V_{606} - I_{814})_b$ (2)	$(V_{606} - I_{814})_d$ (3)	$(V_{606} - I_{814})_g$ (4)	$(U - B)_b$ (5)	$(U - B)_d$ (6)	$(U - B)_g$ (7)	$(B - R)_b$ (8)	$(B - R)_d$ (9)	$(B - R)_g$ (10)
122	1.86 ± 0.16	1.02 ± 0.35	1.29 ± 0.06	0.56	-0.28	-0.01	1.21	0.37	0.65
73	1.25 ± 0.08 ±	1.03 ± 0.04	0.02	-0.20	0.56	0.34
1067	1.38 ± 0.14	1.09 ± 0.25	1.00 ± 0.05	0.11	-0.18	-0.27	0.96	0.67	0.58
1003	1.44 ± 0.09	1.07 ± 0.27	1.10 ± 0.04	0.29	-0.08	-0.04	0.93	0.56	0.59
147	1.17 ± 0.18 ±	1.00 ± 0.05	0.03	-0.15	0.85	0.67

Table A.5. Bulge sample colour gradients

No. (1)	$\nabla(V_{606} - I_{814})_{\text{blue}}$ (2)	$\nabla(V_{606} - I_{814})_{\text{red}}$ (3)	$\nabla(V_{606} - I_{814})_{\text{sma}}$ (4)
1131	0.102 ± 0.020	-0.014 ± 0.051	0.066 ± 0.010
1139	-0.005 ± 0.003	-0.011 ± 0.004	0.022 ± 0.005
1078	-0.017 ± 0.021	-0.028 ± 0.023	-0.014 ± 0.018
1081	-0.030 ± 0.015	-0.049 ± 0.012	-0.012 ± 0.013
1125	-0.024 ± 0.010	-0.034 ± 0.008	-0.038 ± 0.008
139	-0.045 ± 0.010	-0.038 ± 0.018	-0.045 ± 0.018
170	-0.035 ± 0.004	-0.021 ± 0.004	-0.015 ± 0.005
159	-0.013 ± 0.005	-0.020 ± 0.005	-0.017 ± 0.005
1005	0.010 ± 0.021	-0.026 ± 0.013	-0.030 ± 0.017
1099	-0.006 ± 0.008	0.005 ± 0.011	-0.007 ± 0.008
47	-0.005 ± 0.018	-0.018 ± 0.025	-0.015 ± 0.004
1138	-0.002 ± 0.003	-0.020 ± 0.004	-0.007 ± 0.003
1063	-0.021 ± 0.009	-0.016 ± 0.009	-0.029 ± 0.007
1020	0.021 ± 0.012	-0.014 ± 0.011	0.036 ± 0.008
1135	-0.001 ± 0.006	-0.009 ± 0.008	-0.024 ± 0.007
1137	-0.005 ± 0.002	-0.017 ± 0.002	-0.008 ± 0.002
1118	-0.015 ± 0.011	0.017 ± 0.010	0.010 ± 0.008
1142	-0.023 ± 0.003	-0.032 ± 0.005	-0.028 ± 0.003
104	-0.031 ± 0.009	-0.041 ± 0.009	-0.020 ± 0.007
1108	-0.016 ± 0.006	-0.013 ± 0.007	-0.008 ± 0.006
1057	0.035 ± 0.019	-0.006 ± 0.014	0.031 ± 0.013
1046	-0.010 ± 0.015	-0.001 ± 0.023	-0.026 ± 0.009
155	-0.032 ± 0.005	-0.035 ± 0.009	-0.018 ± 0.007
1024	-0.004 ± 0.014	0.007 ± 0.020	-0.000 ± 0.010
1068	-0.036 ± 0.015	-0.051 ± 0.014	-0.025 ± 0.010
123	0.038 ± 0.023	-0.005 ± 0.015	-0.038 ± 0.009
1093	0.012 ± 0.015	-0.005 ± 0.016	0.004 ± 0.016
134	-0.041 ± 0.013	-0.016 ± 0.018	-0.025 ± 0.005
1077	-0.011 ± 0.010	-0.019 ± 0.011	-0.032 ± 0.010
1122	-0.037 ± 0.011	-0.061 ± 0.015	-0.033 ± 0.011
1033	-0.035 ± 0.016	-0.050 ± 0.015	0.053 ± 0.028
1117	-0.020 ± 0.008	-0.008 ± 0.004	-0.010 ± 0.007
110	0.035 ± 0.014	0.010 ± 0.004	-0.008 ± 0.005
162	-0.033 ± 0.010	-0.020 ± 0.004	-0.030 ± 0.006
102	0.004 ± 0.009	-0.039 ± 0.011	-0.001 ± 0.012
1017	-0.024 ± 0.022	-0.051 ± 0.040	-0.046 ± 0.016
116	-0.038 ± 0.018	-0.057 ± 0.011	-0.062 ± 0.010
1113	-0.018 ± 0.004	-0.041 ± 0.004	-0.015 ± 0.004
1083	-0.010 ± 0.009	-0.008 ± 0.010	-0.027 ± 0.005
1115	-0.038 ± 0.012	-0.038 ± 0.006	-0.022 ± 0.013
142	0.067 ± 0.021	0.019 ± 0.014	0.047 ± 0.011
1036	-0.059 ± 0.018	-0.029 ± 0.017	-0.014 ± 0.021
1028	-0.104 ± 0.013	-0.066 ± 0.018	-0.108 ± 0.014
150	-0.024 ± 0.021	-0.043 ± 0.017	-0.032 ± 0.012
1034	-0.018 ± 0.014	0.016 ± 0.012	0.017 ± 0.016
1048	0.014 ± 0.018	-0.031 ± 0.034	-0.015 ± 0.031
8	-0.081 ± 0.022	0.113 ± 0.061	-0.070 ± 0.023
160	-0.015 ± 0.008	-0.016 ± 0.011	-0.029 ± 0.014
1065	-0.014 ± 0.017	-0.018 ± 0.013	-0.001 ± 0.016
1035	0.004 ± 0.027	-0.062 ± 0.018	-0.010 ± 0.024
129	-0.044 ± 0.020	-0.115 ± 0.022	-0.068 ± 0.020
1097	0.030 ± 0.031	-0.065 ± 0.018	-0.085 ± 0.015
59	-0.040 ± 0.022	-0.074 ± 0.027	0.021 ± 0.030
1	-0.068 ± 0.006	-0.060 ± 0.069	0.051 ± 0.036

Table A.6. Non-bulge sample colour gradients

No. (1)	$\nabla(V_{606} - I_{814})_{\text{blue}}$ (2)	$\nabla(V_{606} - I_{814})_{\text{red}}$ (3)	$\nabla(V_{606} - I_{814})_{\text{sma}}$ (4)
86	0.054 ± 0.142	-0.163 ± 0.180	0.331 ± 0.093
1098	0.039 ± 0.044	0.038 ± 0.019	0.069 ± 0.025
133	0.053 ± 0.095	-0.026 ± 0.051	-0.031 ± 0.026
164	0.034 ± 0.033	-0.029 ± 0.033	0.020 ± 0.033
165	0.037 ± 0.018	-0.011 ± 0.026	-0.029 ± 0.010
138	0.085 ± 0.032	0.040 ± 0.040	0.217 ± 0.061
131	-0.000 ± 0.038	0.013 ± 0.027	0.060 ± 0.011
148	0.124 ± 0.052	-0.084 ± 0.062	-0.029 ± 0.027
1025	0.170 ± 0.181	0.033 ± 0.146	-0.263 ± 0.167
9	-0.067 ± 0.085	0.041 ± 0.094	-0.021 ± 0.047
43	-0.112 ± 0.044	-0.259 ± 0.097	-0.093 ± 0.050
157	0.021 ± 0.005	0.028 ± 0.008	0.019 ± 0.006
137	-0.069 ± 0.032	-0.075 ± 0.020	-0.013 ± 0.011
166	0.002 ± 0.015	-0.021 ± 0.020	-0.009 ± 0.005
154	0.017 ± 0.007	0.003 ± 0.015	0.012 ± 0.015
48	0.050 ± 0.051	-0.063 ± 0.041	0.100 ± 0.074
1061	-0.118 ± 0.029	-0.071 ± 0.031	-0.028 ± 0.020
1134	-0.027 ± 0.007	0.003 ± 0.012	-0.016 ± 0.010
1076	-0.079 ± 0.023	-0.011 ± 0.024	-0.077 ± 0.012
1066	-0.045 ± 0.027	-0.118 ± 0.032	0.018 ± 0.021
93	-0.010 ± 0.035	0.010 ± 0.081	-0.086 ± 0.024
1039	-0.372 ± 0.149	-0.027 ± 0.039	-0.052 ± 0.073
1094	-0.066 ± 0.016	-0.067 ± 0.009	-0.039 ± 0.013
169	-0.023 ± 0.004	-0.037 ± 0.004	-0.031 ± 0.004
30	-0.010 ± 0.042	-0.122 ± 0.030	0.003 ± 0.033
163	-0.012 ± 0.011	-0.013 ± 0.011	-0.042 ± 0.003
1088	-0.045 ± 0.006	-0.046 ± 0.013	-0.028 ± 0.009
106	0.005 ± 0.045	-0.050 ± 0.019	0.015 ± 0.017
80	-0.066 ± 0.021	0.032 ± 0.055	-0.081 ± 0.028
75	-0.033 ± 0.015	-0.037 ± 0.018	-0.019 ± 0.021
7	0.107 ± 0.058	0.062 ± 0.022	0.025 ± 0.022
1110	0.011 ± 0.009	-0.004 ± 0.010	0.021 ± 0.007
36	-0.037 ± 0.033	0.119 ± 0.090	0.034 ± 0.042
152	-0.038 ± 0.005	-0.043 ± 0.007	-0.022 ± 0.006
1116	-0.050 ± 0.009	-0.035 ± 0.004	0.028 ± 0.023
1006	0.082 ± 0.024	0.047 ± 0.013	0.057 ± 0.013
1119	-0.025 ± 0.014	-0.005 ± 0.020	-0.011 ± 0.008
1054	0.017 ± 0.043	-0.045 ± 0.045	-0.016 ± 0.033
1141	-0.020 ± 0.004	-0.024 ± 0.003	-0.005 ± 0.005
88	-0.032 ± 0.009	-0.035 ± 0.015	-0.013 ± 0.006
90	-0.042 ± 0.014	-0.010 ± 0.025	0.012 ± 0.020
1074	-0.030 ± 0.010	-0.024 ± 0.011	-0.009 ± 0.012
61	0.000 ± 0.012	-0.052 ± 0.012	-0.010 ± 0.003
1047	-0.006 ± 0.012	0.103 ± 0.048	-0.028 ± 0.030
128	-0.015 ± 0.010	-0.030 ± 0.009	-0.029 ± 0.009
108	-0.020 ± 0.008	-0.025 ± 0.013	-0.028 ± 0.008
1106	-0.032 ± 0.008	-0.045 ± 0.014	-0.034 ± 0.007
140	-0.063 ± 0.016	-0.022 ± 0.011	0.027 ± 0.024
76	-0.038 ± 0.016	0.075 ± 0.031	-0.028 ± 0.018
1055	0.080 ± 0.032	-0.042 ± 0.013	-0.039 ± 0.010
109	-0.020 ± 0.010	0.000 ± 0.014	-0.025 ± 0.011
141	-0.040 ± 0.016	-0.032 ± 0.012	-0.042 ± 0.015
1114	-0.024 ± 0.007	-0.040 ± 0.009	-0.041 ± 0.007
70	-0.024 ± 0.026	-0.006 ± 0.015	-0.042 ± 0.008
91	-0.026 ± 0.020	-0.043 ± 0.027	-0.039 ± 0.019
15	-0.068 ± 0.026	0.060 ± 0.037	0.018 ± 0.023
1100	-0.025 ± 0.013	-0.026 ± 0.023	0.019 ± 0.019
1126	-0.020 ± 0.004	0.001 ± 0.010	-0.038 ± 0.007
66	-0.022 ± 0.024	-0.026 ± 0.022	-0.025 ± 0.019
1042	0.035 ± 0.047	-0.016 ± 0.032	-0.053 ± 0.023
1136	-0.027 ± 0.010	-0.031 ± 0.007	-0.035 ± 0.007
1029	-0.044 ± 0.008	-0.006 ± 0.020	0.008 ± 0.022
1133	-0.010 ± 0.005	-0.011 ± 0.013	-0.027 ± 0.006
17	-0.077 ± 0.006	-0.007 ± 0.021	0.009 ± 0.025
1103	-0.024 ± 0.012	-0.050 ± 0.013	-0.053 ± 0.011
117	-0.025 ± 0.016	-0.065 ± 0.016	-0.038 ± 0.019

Table A.6. Continued.

No. (1)	$\nabla(V_{606} - I_{814})_{\text{blue}}$ (2)	$\nabla(V_{606} - I_{814})_{\text{red}}$ (3)	$\nabla(V_{606} - I_{814})_{\text{sma}}$ (4)
125	-0.028 ± 0.017	0.066 ± 0.009	-0.020 ± 0.011
113	-0.064 ± 0.009	-0.047 ± 0.013	-0.054 ± 0.011
1043	-0.047 ± 0.049	-0.020 ± 0.005	0.059 ± 0.028
34	-0.125 ± 0.078	-0.059 ± 0.045	-0.026 ± 0.037
112	-0.003 ± 0.012	0.056 ± 0.033	0.003 ± 0.013
64	-0.025 ± 0.024	-0.016 ± 0.029	-0.005 ± 0.012
1107	-0.017 ± 0.014	-0.017 ± 0.017	-0.010 ± 0.018
42	-0.060 ± 0.016	-0.023 ± 0.022	-0.039 ± 0.010
69	-0.075 ± 0.008	-0.028 ± 0.018	-0.086 ± 0.017
1121	-0.034 ± 0.033	-0.043 ± 0.016	-0.077 ± 0.018
1044	-0.010 ± 0.020	-0.034 ± 0.026	-0.008 ± 0.019
32	-0.027 ± 0.021	0.030 ± 0.026	-0.011 ± 0.014
1037	-0.052 ± 0.011	0.029 ± 0.035	-0.090 ± 0.020
3	-0.018 ± 0.028	-0.057 ± 0.053	-0.033 ± 0.033
105	-0.088 ± 0.025	-0.030 ± 0.010	-0.050 ± 0.013
23	-0.071 ± 0.034	0.052 ± 0.040	0.018 ± 0.025
1053	-0.029 ± 0.009	-0.066 ± 0.016	-0.028 ± 0.012
158	-0.021 ± 0.013	-0.034 ± 0.011	-0.020 ± 0.006
49	0.004 ± 0.032	-0.002 ± 0.020	-0.049 ± 0.021
11	0.068 ± 0.030	-0.022 ± 0.028	-0.007 ± 0.014
149	-0.004 ± 0.011	-0.045 ± 0.008	-0.027 ± 0.015
136	-0.037 ± 0.007	0.004 ± 0.014	-0.033 ± 0.009
46	-0.096 ± 0.044	-0.042 ± 0.019	-0.071 ± 0.011
146	-0.031 ± 0.014	-0.044 ± 0.020	-0.031 ± 0.062
1016	-0.027 ± 0.032	-0.021 ± 0.015	0.014 ± 0.019
1123	-0.033 ± 0.007	-0.052 ± 0.011	-0.017 ± 0.007
1102	-0.011 ± 0.009	-0.006 ± 0.012	-0.023 ± 0.009
1031	-0.045 ± 0.020	-0.018 ± 0.042	-0.018 ± 0.031
1090	-0.030 ± 0.010	-0.032 ± 0.017	-0.014 ± 0.015
94	-0.086 ± 0.012	-0.085 ± 0.040	-0.036 ± 0.026
132	-0.019 ± 0.016	-0.072 ± 0.028	-0.036 ± 0.024
84	-0.008 ± 0.020	-0.007 ± 0.019	0.019 ± 0.022
74	0.006 ± 0.022	-0.061 ± 0.017	-0.025 ± 0.021
20	-0.098 ± 0.023	-0.021 ± 0.041	-0.005 ± 0.025
40	-0.116 ± 0.048	-0.026 ± 0.039	-0.050 ± 0.033
96	-0.035 ± 0.022	-0.034 ± 0.023	0.002 ± 0.012
1127	-0.036 ± 0.015	-0.035 ± 0.021	-0.079 ± 0.035
1009	-0.053 ± 0.018	-0.009 ± 0.027	-0.028 ± 0.026
156	-0.070 ± 0.022	-0.052 ± 0.011	-0.089 ± 0.009
1082	-0.076 ± 0.007	-0.050 ± 0.016	-0.061 ± 0.021
126	-0.006 ± 0.017	0.053 ± 0.022	0.019 ± 0.060
65	-0.092 ± 0.044	0.016 ± 0.019	-0.020 ± 0.024
39	-0.069 ± 0.053	-0.030 ± 0.020	-0.022 ± 0.019
1095	-0.038 ± 0.015	-0.020 ± 0.028	-0.024 ± 0.029
1084	-0.055 ± 0.026	-0.023 ± 0.021	-0.051 ± 0.024
55	-0.086 ± 0.027	-0.016 ± 0.016	-0.120 ± 0.022
1019	-0.107 ± 0.025	-0.063 ± 0.018	-0.062 ± 0.030
1079	-0.013 ± 0.023	-0.065 ± 0.016	-0.076 ± 0.011
57	-0.105 ± 0.041	-0.002 ± 0.034	-0.013 ± 0.022
1023	-0.080 ± 0.048	-0.550 ± 0.108	-0.249 ± 0.064
1064	0.013 ± 0.015	-0.045 ± 0.030	-0.014 ± 0.009
1021	-0.104 ± 0.038	0.054 ± 0.058	-0.125 ± 0.064
1004	0.054 ± 0.044	0.054 ± 0.032	0.072 ± 0.028
1062	-0.021 ± 0.017	-0.025 ± 0.029	-0.042 ± 0.027
14	-0.113 ± 0.021	0.030 ± 0.048	-0.140 ± 0.037
58	0.026 ± 0.015	0.020 ± 0.037	-0.127 ± 0.084
26	0.050 ± 0.012	-0.001 ± 0.018	0.016 ± 0.016
16	0.022 ± 0.030	0.028 ± 0.049	-0.049 ± 0.014
1091	0.069 ± 0.061	-0.044 ± 0.065	0.088 ± 0.014
1001	-0.087 ± 0.020	-0.055 ± 0.025	-0.021 ± 0.022
114	-0.000 ± 0.022	0.057 ± 0.018	-0.058 ± 0.032
1045	-0.024 ± 0.047	-0.122 ± 0.030	-0.047 ± 0.119
1092	-0.193 ± 0.020	-0.102 ± 0.018	-0.099 ± 0.041
19	0.072 ± 0.043	0.027 ± 0.021	-0.012 ± 0.022
85	-0.010 ± 0.101	-0.024 ± 0.017	-0.029 ± 0.014
21	-0.043 ± 0.025	0.097 ± 0.035	-0.123 ± 0.048

Table A.6. Continued.

No. (1)	$\nabla(V_{606} - I_{814})_{\text{blue}}$ (2)	$\nabla(V_{606} - I_{814})_{\text{red}}$ (3)	$\nabla(V_{606} - I_{814})_{\text{sma}}$ (4)
122	-0.052 ± 0.042	0.074 ± 0.077	-0.119 ± 0.023
73	-0.043 ± 0.020	-0.056 ± 0.013	-0.060 ± 0.027
1067	0.063 ± 0.050	0.013 ± 0.029	0.083 ± 0.073
1003	-0.106 ± 0.032	-0.096 ± 0.025	-0.075 ± 0.017
147	0.027 ± 0.036	-0.023 ± 0.020	-0.032 ± 0.014

Appendix B: Sample of galaxies with bulges

Notes for figures:

Column (1): 10×10 arcsec postage stamp of the source in $F814W$ band

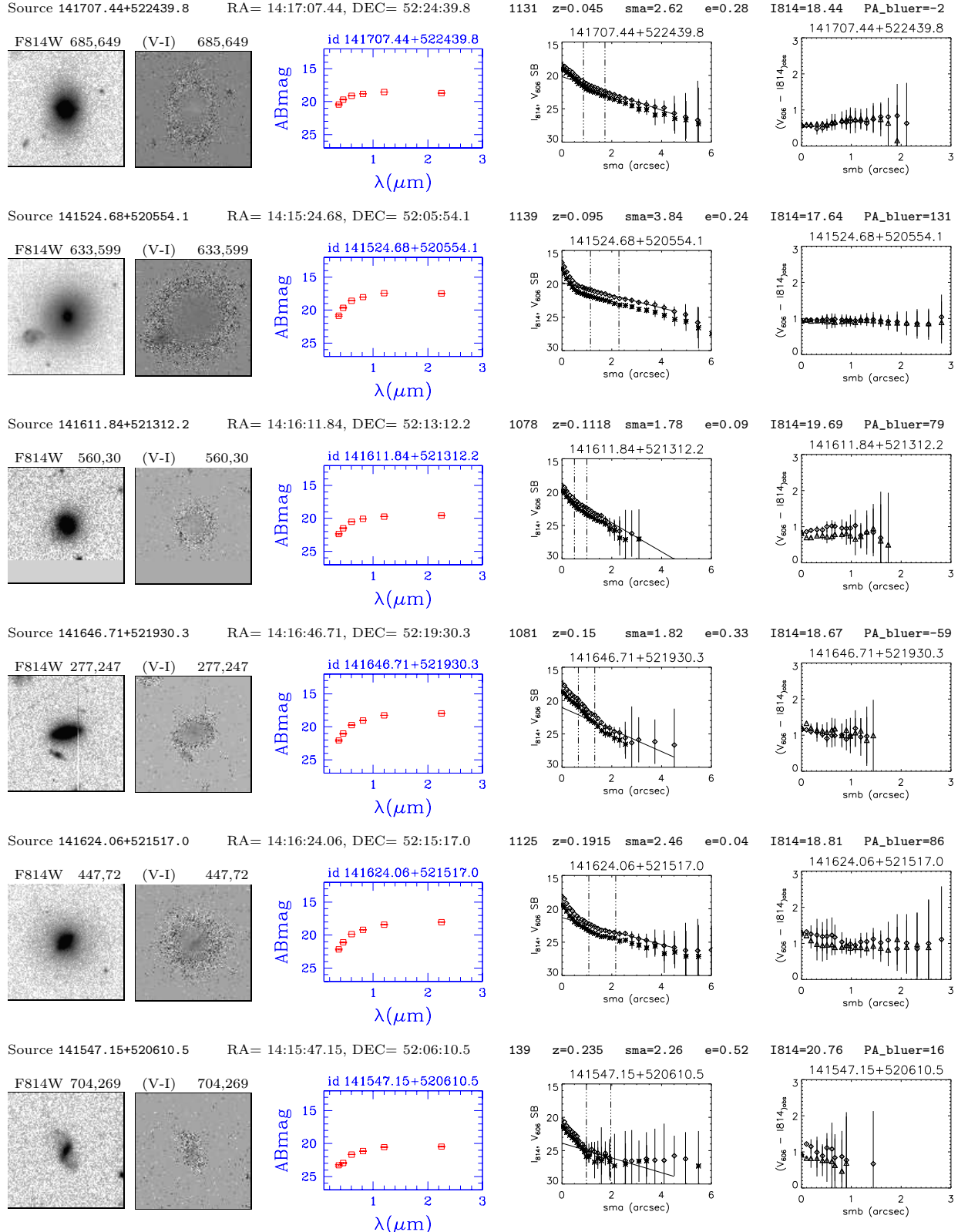
Column (2): 10×10 arcsec postage stamp of the observed ($F606W - F814W$) colour map

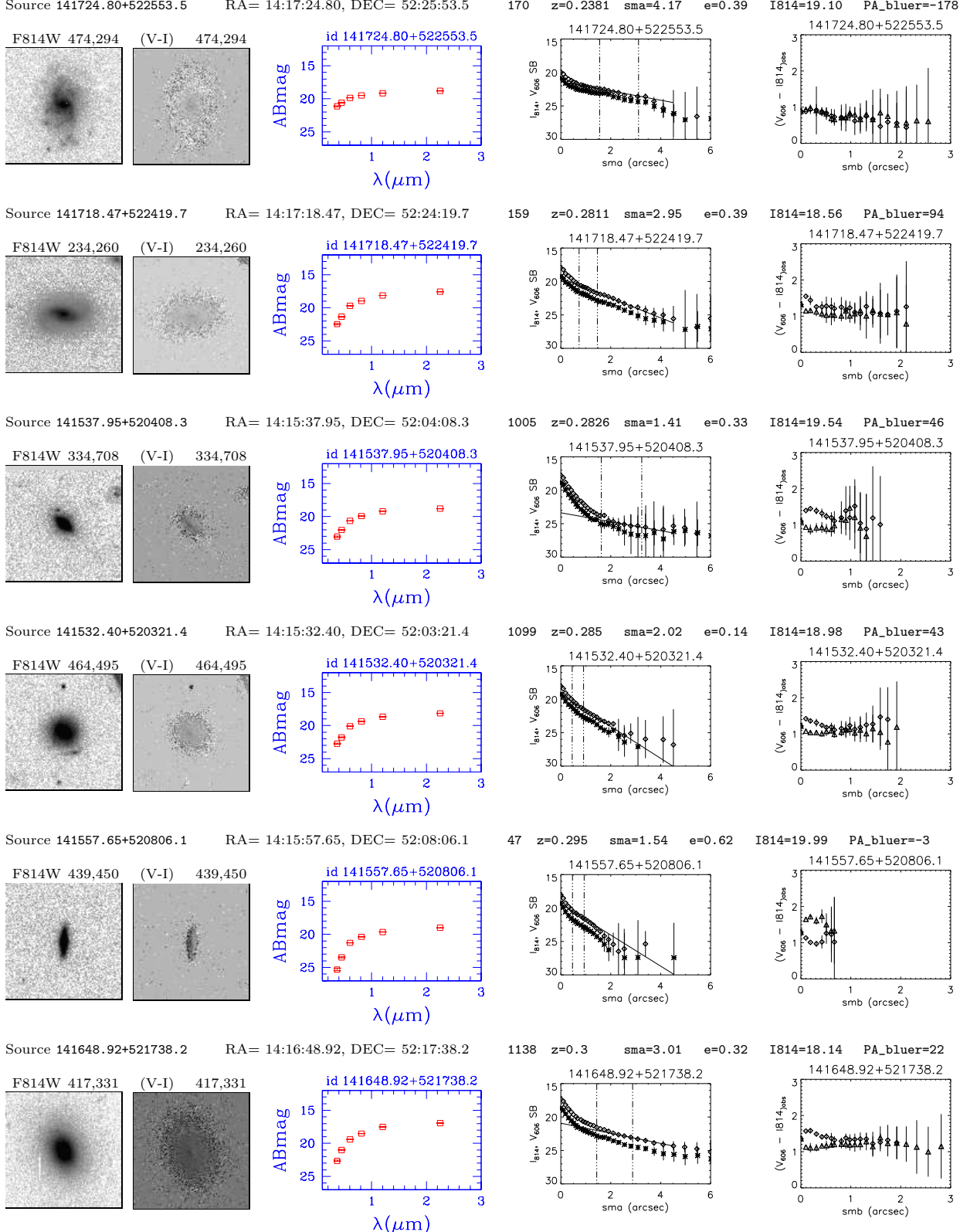
Column (3): Photometric spectral energy distribution

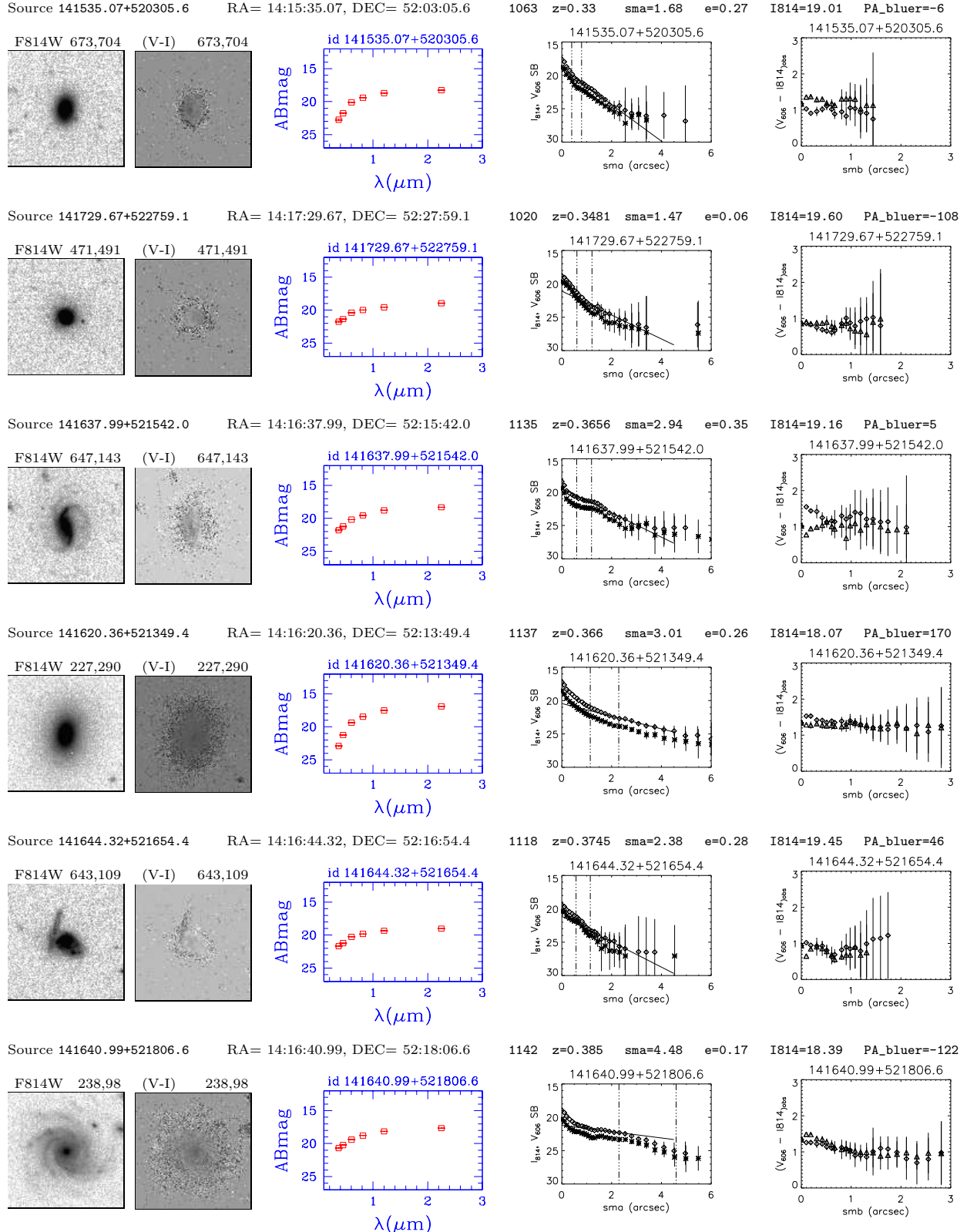
Column (4): Averaged surface brightness profile along both semi-major axis for $F814W$ and $F606W$ bands. *Solid line*: exponential law fitted to the outer region of the galaxy. *Vertical dashed lines*: 1 and 2 times the scale length of the exponential fit; this is the range in which disk colours were measured

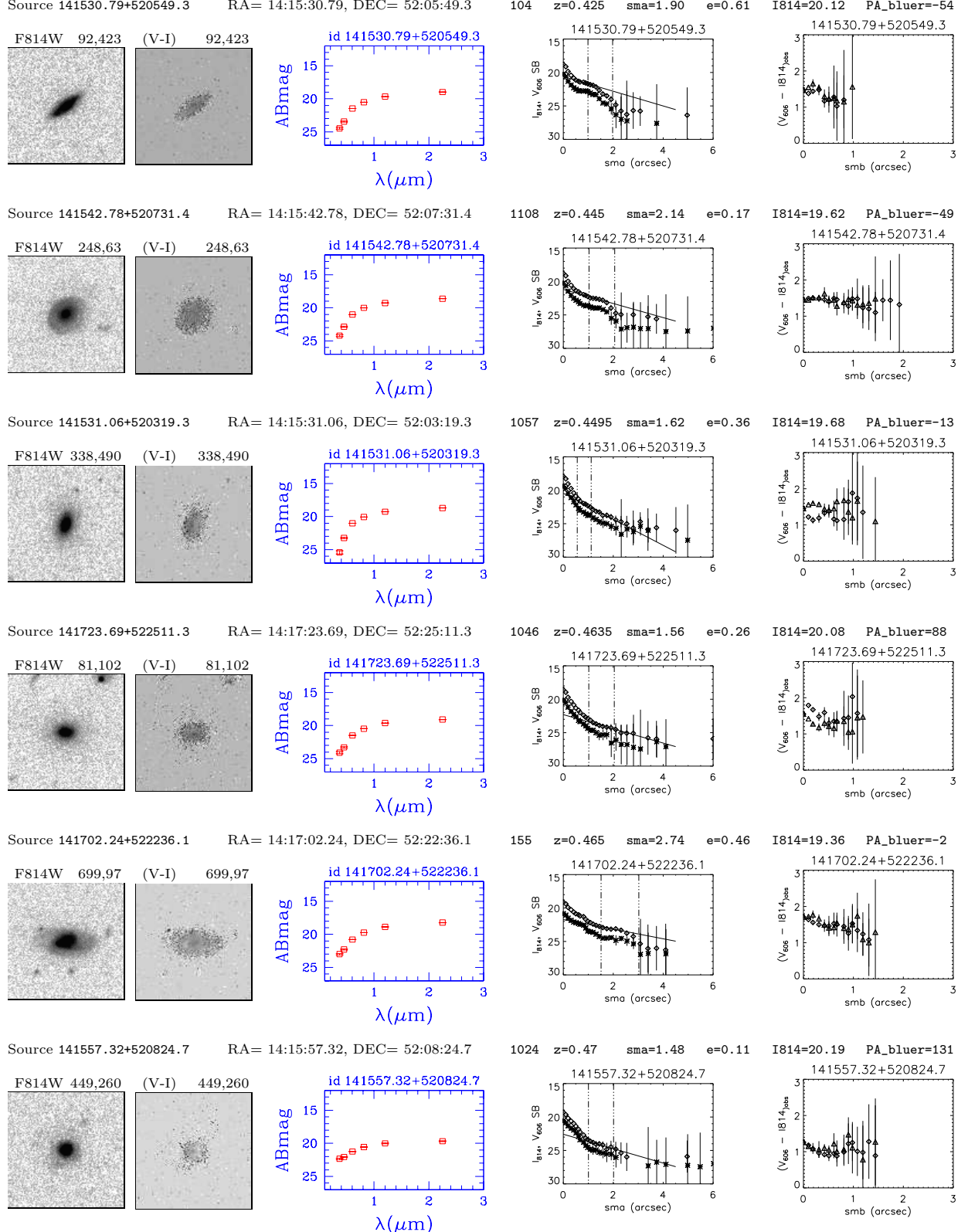
Column (5): Observed colour profiles, ($F814W - F606W$), over both semi-minor axes.

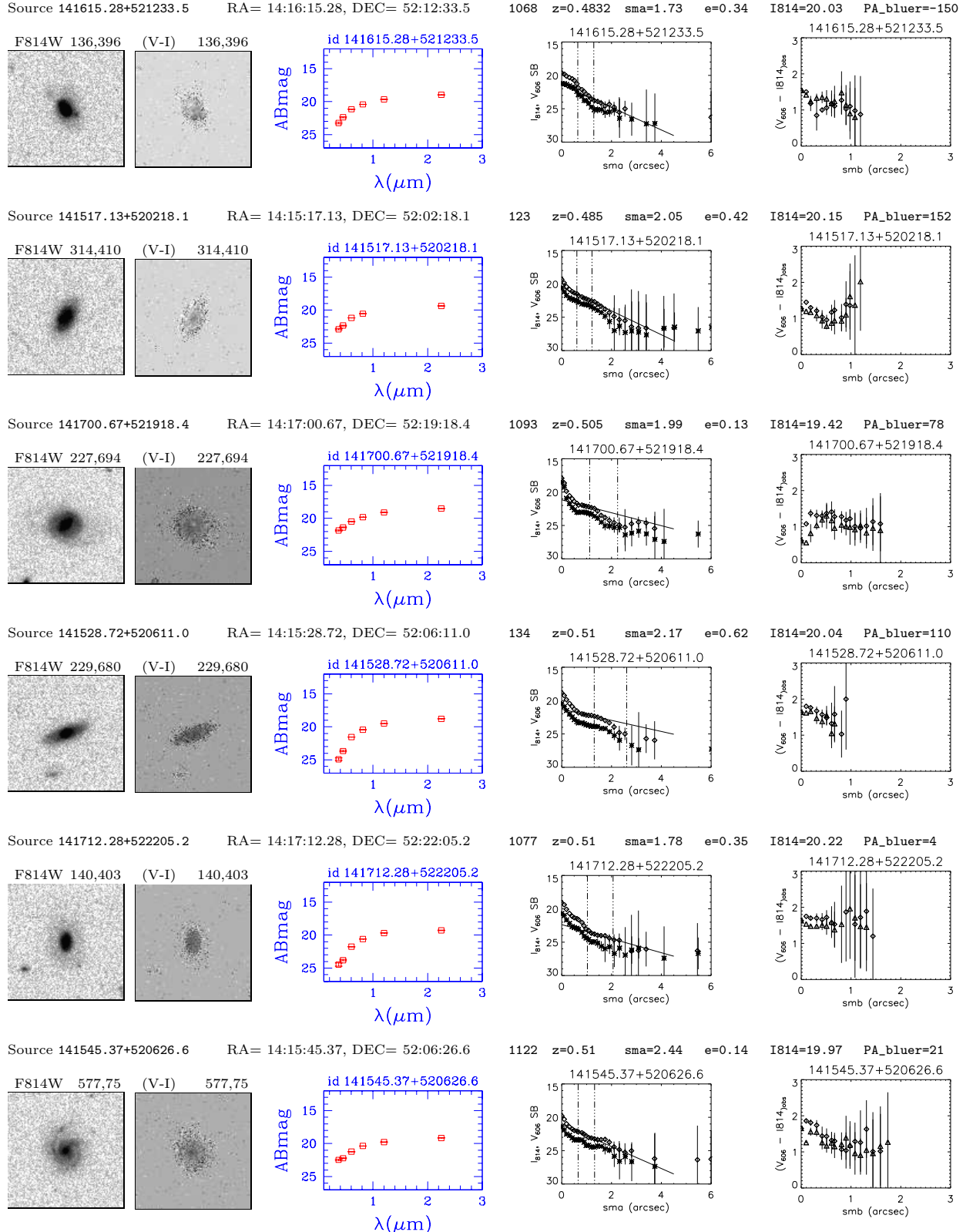
Note: On top of each row we list: the source ID; the source sky coordinates, right ascension and declination (RA, DEC, J2000.0); the source number identification; the source redshift (z), either photometric or spectroscopic; the semi-major axis (sma); the ellipticity (e); and, the position angle of the bluer semi-minor axis in which we measure nuclear colours, counter clockwise from the horizontal axis (PA.bluer).

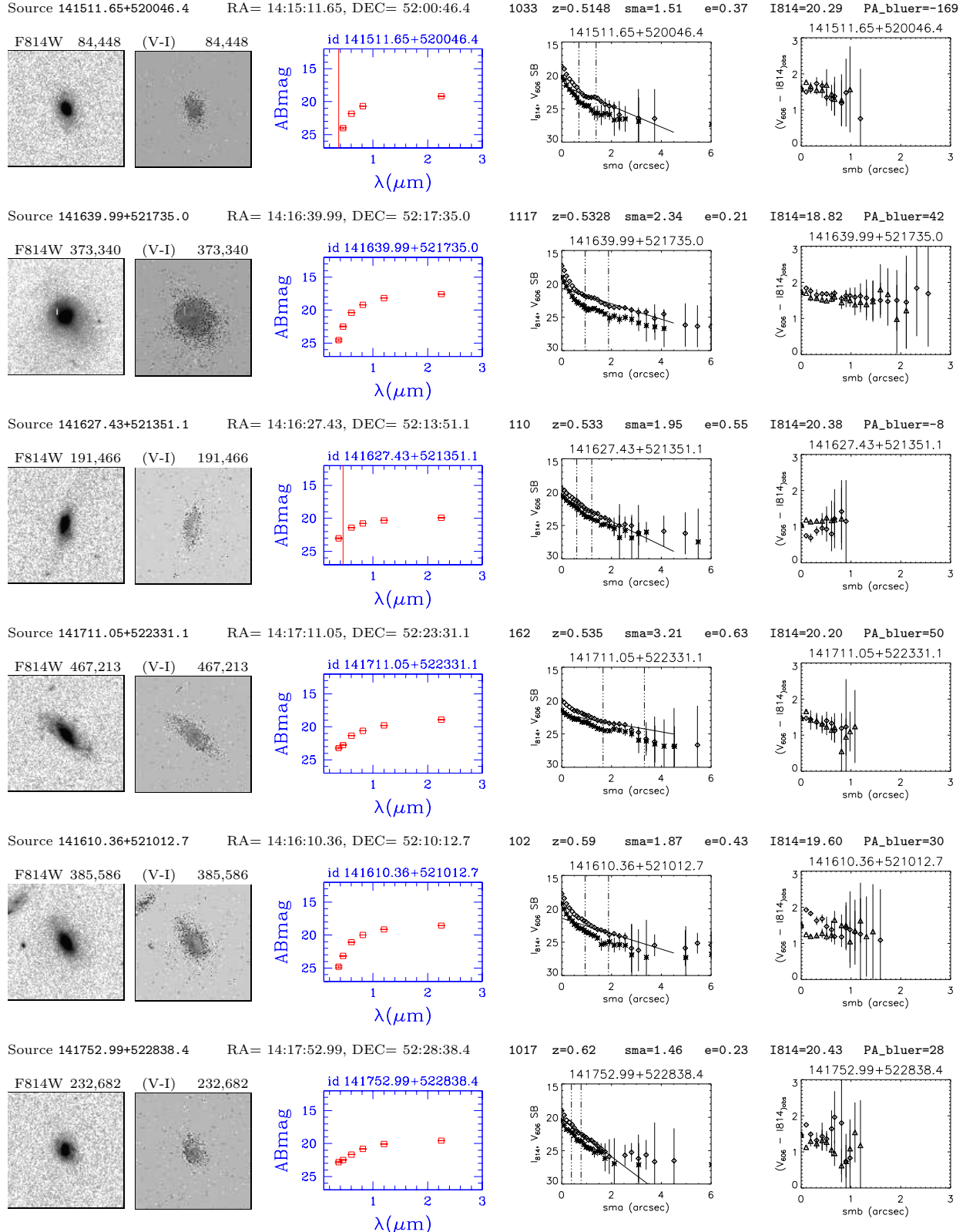


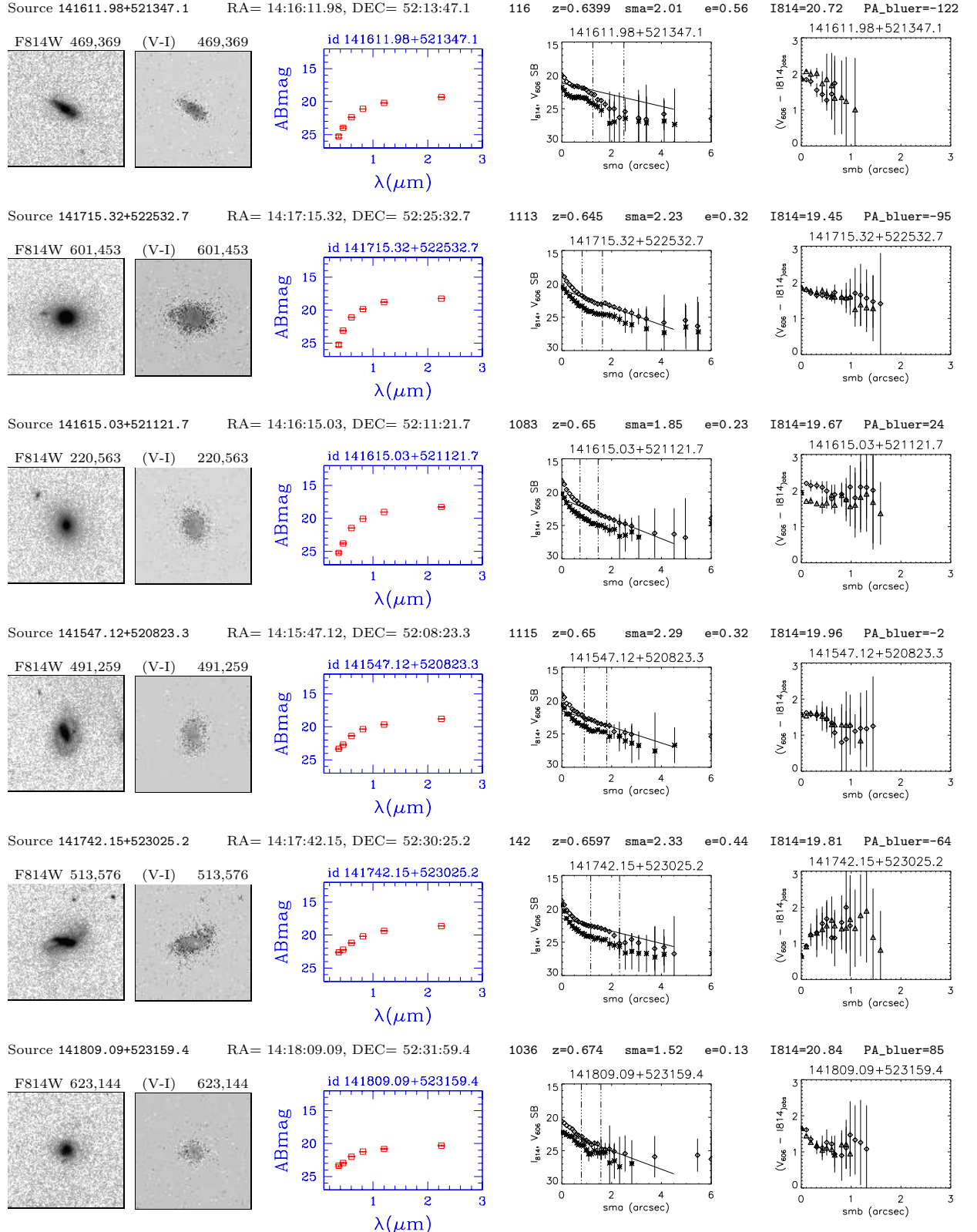


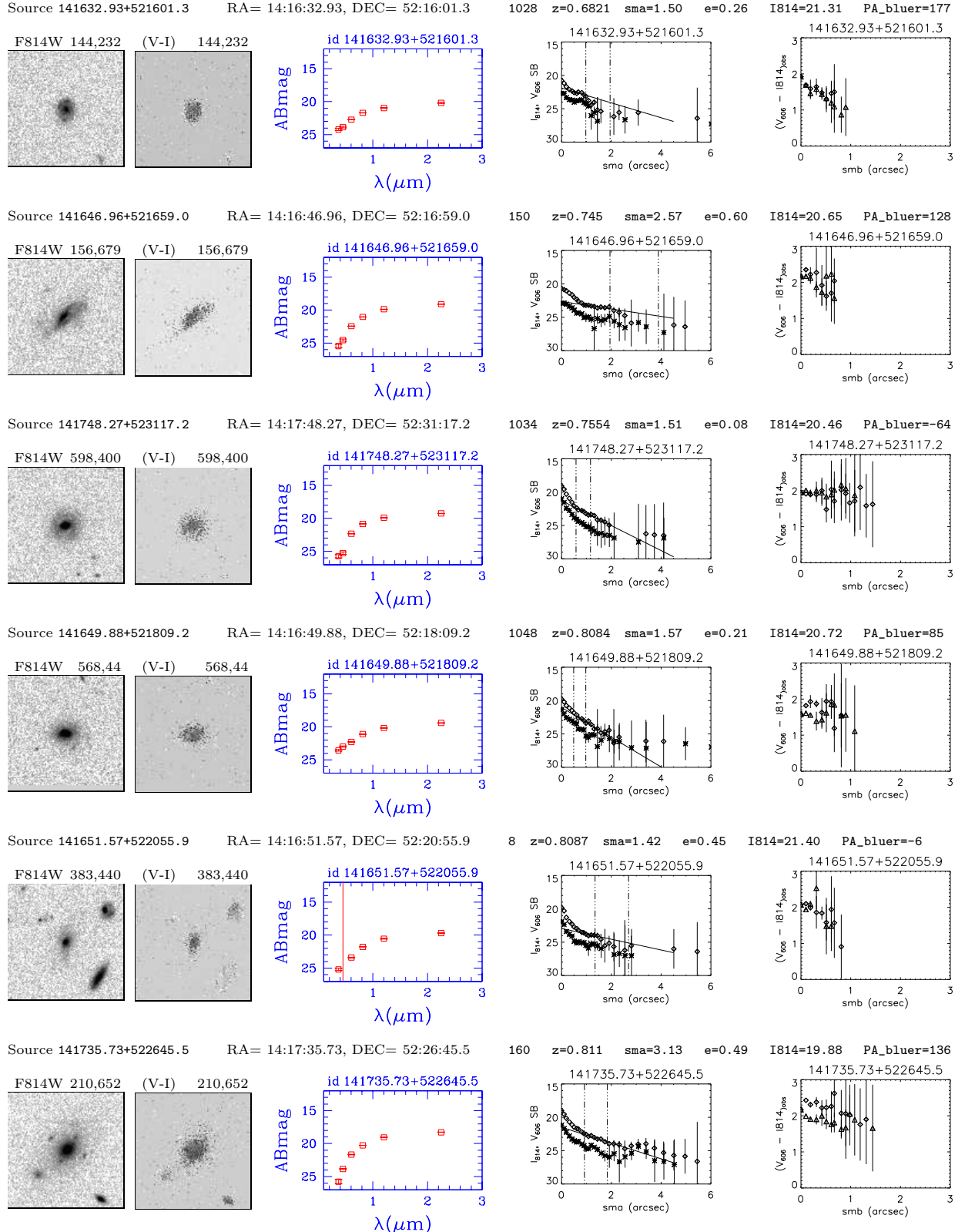


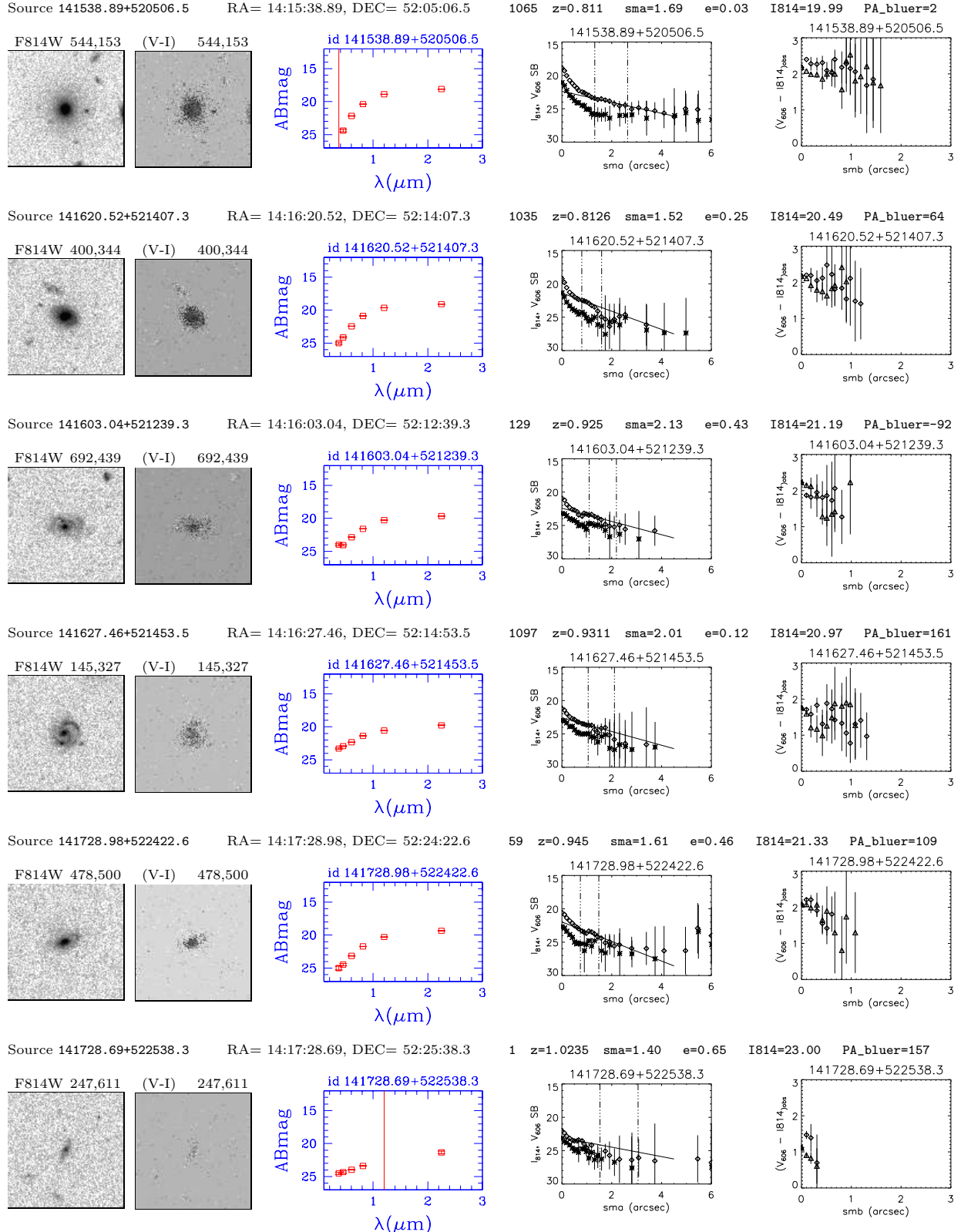












Appendix C: Colour profiles in bluer semi-minor axes

Notes for Figures C:

The ($F606W - F814W$) colour profiles along the bluer deprojected semi-minor axes colour profile, for the bulge and the non-bulge samples. Overplotted are the linear fits done to calculate the colour gradients. The profiles are ordered from top to bottom as in the Appendices A and B. Minor tick marks on the y-axis correspond to 1 mag in ($F606W - F814W$).

